Nuclear Structure of Na²². I. Gamma-Ray Correlations and Lifetime Measurements for Levels of $E_{\rm ex} < 3.1$ MeV*

E. K. WARBURTON, J. W. OLNESS, AND A. R. POLETTI

Brookhaven National Laboratory, Upton, New York

(Received 17 March 1967)

Levels of Na²² below an excitation energy of 3.1 MeV have been investigated through the $F^{19}(\alpha,n\gamma)Na^{22}$ and $Ne^{20}(He^3,p\gamma)Na^{22}$ reactions. Gamma-ray spectra from the first reaction were recorded with an 8-cc Ge(Li) detector at 90°, 0°, and 166° to the α beam using CaF₂ targets and α energies between 4.0 and 7.0 MeV. Spectra were similarly recorded at 90° for $E_{He^3} = 5.65$ MeV in the second reaction. These studies were supplemented by γ-γ coincidence measurements with both NaI(Tl)-NaI(Tl) and NaI(Tl)-Ge(Li) γ-ray detector combinations. Gamma-ray angular distributions were measured at $E_\alpha = 5.48$ MeV using the $F^{19}(\alpha,n)Na^{22}$ reaction and p-γ angular correlations were measured at $E_{He^3} = 5.65$ MeV using the $Ne^{20}(He^3,p)Na^{22}$ reaction. From these measurements excitation energies and γ-ray decay modes were determined for the levels below 3.1-MeV excitation, information on spin-parity and isotopic-spin assignments was obtained, and values or limits for the mean lifetimes of the levels were extracted from observations of the γ-ray Doppler shifts. An isotopic-spin assignment of $T = 1$ was made to the Na²² 1.952-MeV level; all other levels in the range $0.7 < E_x (\text{MeV}) < 3.1$ were assigned $T = 0$. Upon combining our results with previously available information, we deduce the following spin-parity and lifetime information $\{E_{\rm ex}(\text{MeV})[J^\pi; \tau_m(\text{psec})]\}$ for the third through eleventh levels of Na²²: 0.891 (4⁺; >8), 1.528 (3⁺, 5⁺; 3.8±0.9), 1.937 (1⁺; <0.06), 1.952 (1, 2; <0.09), 1.984 (2⁺, 3⁺; 1.6±0.34), 2.211 (1; >11), 2.572 (≤3; >10), 2.969 (≤3; <0.14), 3.059 (≤3; <0.09). The combined influence of Doppler effects and the lifetimes of the initial states on the shapes of the full-energy-loss peaks of the 1.528 → 0 and 1.984 → 0.583 transitions is quite marked. The analysis of these shapes to obtain the lifetimes given above is described in detail. Some incidental information concerning excitation energies and lifetimes of energy levels in F¹⁹ and Ne²² is given in an Appendix.

I. INTRODUCTION

ACCORDING to the nuclear shell model Na²² consists, in first order, of six particles in the $2s$-$1d$ shell outside of the doubly closed $1p$ shell (O¹⁶). It lies in a region of the $2s$-$1d$ shell where collective effects are quite apparent and where the simplified unified model has been rather successful.[1] A relatively crude form of the unified model has been applied in the region $20 \leqslant A \leqslant 23$ and, although it has provided a useful orientation, it is desirable to treat these nuclei in a less approximate manner. This is especially true for Na²² which has been treated only casually by the unified model.[2,3] What appears possible in the near future is a comprehensive shell-model treatment, including in an appropriate way those interactions which give rise to collective effects. Theoretical treatments of Na²² which have a complexity somewhere between the unified model treatment and such comprehensive shell-model calculations have recently been reported.[4,5] Because of the difficulty of the theoretical treatments, which are now possible as well as desirable, it is important to have as complete an experimental description of Na²² as possible before such calculations are undertaken.

Experimental information concerning the bound states of Na²² is quite incomplete. Of the 50 levels observed[6] below the proton binding energy of 6.743 MeV[7] only the ground state and first three excited states had been assigned definite spin, parity, and isotopic spin at the time this work was commenced.[2,7,8]

In this report we are concerned with properties of the first 11 excited states of Na²². The information on the quantum numbers of the first 16 levels available prior to the present work is shown in Fig. 1. Also included in this figure is the presently known information[9,10] concerning the pertinent region of excitation energy for Ne²², the $T_z = 1$ member of the isotopic-spin triad of which Na²² is the $T_z = 0$ member. An excitation energy of 3.357 ± 0.002 MeV for the second-excited state of Ne²² was obtained as an incidental by-product of the present work (see Appendix C). This result is incorporated in Fig. 1.

The excitation energies given in Fig. 1 for the Na²² levels below 3.1-MeV excitation are from the present investigation. They are in good agreement with values quoted from previous studies,[6,7] but are considerably

* Work performed under the auspices of the U. S. Atomic Energy Commission.

[1] A. E. Litherland, H. McManus, E. B. Paul, D. A. Bromley, and H. E. Gove, Can. J. Phys. **36**, 378 (1958); A. J. Howard, J. P. Allen, and D. A. Bromley, Phys. Rev. **139**, B1135 (1965). These papers between them give a fairly complete list of the relevant earlier references.

[2] H. J. Maier, D. Pelte, J. G. Pronko, and C. Rolfs, Nucl. Phys. **84**, 1 (1966).

[3] E. B. Paul, private communication quoted in Ref. 2; G. Rakavy, Nucl. Phys. **4**, 375 (1957); D. M. Brink and A. K. Kerman, *ibid.* **12**, 314 (1959).

[4] A. Arima, in Proceedings of the Second Symposium on the Structure of Low-Medium Mass Nuclei, edited by P. Goldhammer and L. W. Seagondollar (unpublished).

[5] B. H. Wildenthal, P. W. M. Glaudemans, E. C. Halbert, and J. B. McGrory, Bull. Am. Phys. Soc. **12**, 48 (1967); also (private communication).

[6] S. Hinds, H. Marchant, and R. Middleton, Nucl. Phys. **51**, 427 (1964).

[7] P. M. Endt and C. Van der Leun, Nucl. Phys. **34**, 1 (1962).

[8] G. T. Carola, M.S. thesis, University of Alberta, Edmonton, Canada, 1965 (unpublished).

[9] D. Pelte, B. Povh, and W. Scholz, Nucl. Phys. **52**, 333 (1964), S. Buhl, D. Pelte, and B. Povh, *ibid.* **A91**, 319 (1967).

[10] C. Broude and M. A. Eswaran, Can. J. Phys. **42**, 1300 (1964); M. A. Eswaran and C. Broude, *ibid.* **42**, 1311 (1964).
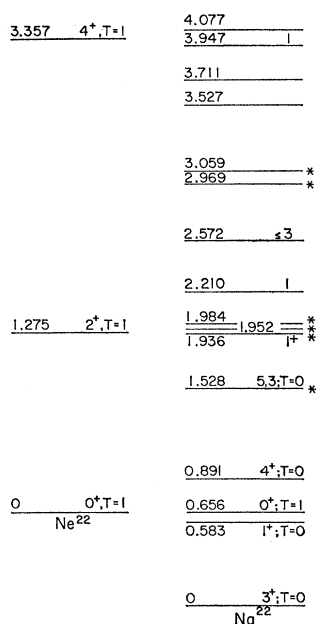
3.357   4⁺,T=1

4.077
3.947   1
3.711
3.527

3.059   *
2.969   *

2.572   ≤3

2.210   1

1.984
——— 1.952   *
1.936   1⁺   *

1.275   2⁺,T=1

1.528   5,3;T=0 *

0.891   4⁺;T=0

0   0⁺,T=1
Ne²²

0.656   0⁺;T=1
0.583   1⁺;T=0

0   3⁺;T=0
Na²²

FIG. 1. The low-lying energy levels of Na²² and Ne²². The excitation energies of the Na²² levels below 3.1-MeV excitation are from the present work, those above 3.1-MeV excitation are from Ref. 6. The spin-parity and isotopic-spin assignments for the Na²² levels are from data reviewed in Refs. 2 and 7. The data for Ne²² are from Refs. 9 and 10. The energy levels of Ne²² are displaced to display the correspondence between isotopic-spin analog states. An asterisk denotes those Na²² levels for which the present work results in new information concerning spin, parity, and isotopic-spin quantum numbers.

more accurate (see Sec. II). The excitation energies for levels above 3.1-MeV excitation are from the work of Hinds et al.[6] The Na²² spin-parity and isotopic-spin assignments of Fig. 1 are from results presented or reviewed by Maier et al.[2] with the exception of those for the 1.937-MeV level which has recently been assigned[11] $J^\pi=1^+$ on the basis of its γ-ray decay to the 0⁺, 0.657-MeV level and the logft value for the β decay to it of the 0⁺, Mg²² ground state.

The purpose of the present work was to gain further information on the quantum numbers and on electromagnetic decay rates of the states between 0.8- and 3.1-MeV excitation in Na²². (Work is in progress on the states above 3.1 MeV.[12]) A variety of methods was used to study these states. In preliminary surveys γ-spectra from the $F^{19}(\alpha,n)Na^{22}$, $Ne^{20}(He^3,p)Na^{22}$, and $Na^{23}(He^3,\alpha)Na^{22}$ reactions were studied with a Ge(Li) spectrometer. We found that the last reaction was quite inferior to the first two since the yield was considerably lower and was small compared to competing reactions, such as $Na^{23}(He^3,p)Mg^{25}$ and $Na^{23}(He^3,n)Al^{25}$. Numerous γ-ray singles spectra and γ-γ coincidence spectra were then recorded under different conditions for both the $F^{19}+\alpha$ and $Ne^{20}+He^3$ reactions. This work is described

in Sec. II. Gamma-ray angular distribution studies using the $F^{19}(\alpha,n)Na^{22}$ reaction are presented in Sec. III. Particle-γ angular correlation studies of the third through eighth excited states of Na²² using the Ne^{20}-$(He^3,p)Na^{22}$ reaction are presented in Sec. IV. Investigations of the lifetimes of the third through eleventh excited states using the $F^{19}(\alpha,n)Na^{22}$ reaction are described in Sec. V. Finally, the results of this and previous work are collected and discussed in Sec. VI.

II. EXCITATION ENERGIES AND DECAY MODES OF THE LOW-LYING LEVELS OF Na²²

The $Ne^{20}(He^3,p)Na^{22}$ and $F^{19}(\alpha,n)Na^{22}$ reactions have Q values of 5.784 and -1.949 MeV, respectively. These reactions were initiated by doubly-ionized He³ and He⁴ beams from the BNL 3.5-MV electrostatic accelerator. Ion energies between 4 and 7 MeV were used at various times.

The Ne²⁰ target consisted of enriched Ne²⁰ gas[13] confined by a 0.1-mil nickel window at a pressure of 0.6 atm. The F¹⁹ targets were in the form of CaF₂ evaporated onto nickel backings. The thickness of the CaF₂ targets varied from 0.02 to 1.0 mg/cm². Excitation energies and information on γ-ray decay modes were obtained from γ-ray singles spectra measured with an 8-cc Ge(Li) detector. The detector had a resolution [full width at half-maximum (FWHM)] of between 3.5 and 4.5 keV (depending on experimental conditions) for full-energy-loss peaks with energies less than 2 MeV. The spectra were recorded using either a 4096-channel digitally stabilized analog-to-digital converter (ADC) or a 1024-channel ADC in conjunction with a Technical Measurement Corporation (TMC) 16 384-channel pulse-height analyzer.

In addition to these singles spectra, γ-γ coincidence spectra of two different types were recorded for both reactions. The first type comprised conventional NaI(Tl)-NaI(Tl) two-parameter coincidence spectra recorded using the 128×128-channel mode of the 16 384-channel analyzer. The second type consisted of Ge(Li) spectra recorded in coincidence with various γ-ray lines viewed by a 3×3-in. NaI(Tl) γ-ray detector. In these latter measurements eight 1024-channel Ge(Li) spectra were recorded simultaneously using the model 245 "spectrum sorter" facility of the TMC 16 384-channel analyzer. The experimental procedures and methods of analysis used at this laboratory for these two types of γ-γ coincidence studies have been described previously.[14,15] The NaI(Tl)-Ge(Li) coincidence spectra served to confirm the major branches established by the NaI(Tl)-NaI(Tl) results. They were

[11] A. Gallmann, G. Frick, E. K. Warburton, D. E. Alburger, and S. Hechtl, Phys. Rev. (to be published).

[12] A. R. Poletti, J. W. Olness, and E. K. Warburton, Phys. Rev. (to be published).

[13] The enriched Ne²⁰ gas had an isotopic purity of 99.99%. It was provided through the courtesy of Dr. A. J. Howard. See A. J. Howard and W. W. Watson, J. Chem. Phys. **40**, 1409 (1964).

[14] E. K. Warburton, J. W. Olness, and D. E. Alburger, Phys. Rev. **140**, B1202 (1965).

[15] E. K. Warburton, J. W. Olness, and A. R. Poletti, Phys. Rev. **155**, 1164 (1967).

particularly useful in resolving close-lying γ rays or in identifying particular γ-ray lines. For those cases where the energy resolution of the NaI(Tl) detectors permitted, the NaI(Tl)-NaI(Tl) results gave stricter upper limits on nonobserved transitions than the Ge(Li)-NaI(Tl) results. This was due mainly to improved counting statistics resulting from the greater detector efficiency. Since these γ-γ coincidence measurements served primarily to confirm the singles measurements, and yielded very little independent information of a positive nature, we shall not present any of this coincidence data explicitly, but shall concentrate on the singles measurements.

The $F^{19}(\alpha,n\gamma)Na^{22}$ reaction proved to be a more suitable reaction for studying the low-lying levels of Na^{22} via singles measurements than the $Ne^{20}(He^3,p\gamma)$-Na^{22} reaction for the reasons discussed below. Thus we shall present data from the former reaction only; although we note that *all* the Na^{22} γ rays identified in this section were observed in both reactions and that the excitation energies and branching ratios extracted via the $Ne^{20}(He^3,p\gamma)Na^{22}$ reaction were consistent with those obtained from the $F^{19}(\alpha,n\gamma)Na^{22}$ reaction.

Because of the relatively high Q value of the Ne^{20}-$(He^3,p)Na^{22}$ reaction, it is possible to form all of the bound states of Na^{22} by this reaction with $E_{He^3}\gtrsim 5$ MeV. Also, all of the bound states of Ne^{19} can be formed by the $Ne^{20}(He^3,\alpha)Ne^{19}$ reaction ($Q=3.702$ MeV). Thus it was not surprising to find that $Ne^{20}+He^3$ was a rich source of γ rays: The γ-ray lines originating from the low-lying states of Na^{22} were superimposed on a high background resulting from the continuum due to more energetic γ rays, and were intermingled with γ-ray lines originating from higher-lying states of Na^{22} and from levels of Ne^{19}.

In contrast, γ rays from the low-lying levels of Na^{22} dominated the γ-spectra from $F^{19}+\alpha$. Since the F^{19}-$(\alpha,n)Na^{22}$ reaction is endothermic ($Q=-1.949$ MeV), the formation of Na^{22} states could be controlled by varying the beam energy. This feature of endothermic reactions aided in the identification of the γ-ray lines and allowed the "peak-to-background" ratio for particular γ rays to be approximately maximized. For present purposes a second advantage of the $F^{19}(\alpha,n)Na^{22}$ reaction over the $Ne^{20}(He^3,p)Na^{22}$ reaction results from the fact that the former was initiated in a solid target and the latter in a gaseous target. The stopping times of the recoiling Na^{22} ions in gas and solid targets are of the order of 5×10^{-10} and 5×10^{-13} sec, respectively, and a good many of the Na^{22} states studied have mean lifetimes between these two values. Thus, almost all of the γ-ray lines observed from $Ne^{20}+He^3$ were Doppler broadened while many of those observed from $F^{19}+\alpha$ were not. Consequently the γ-ray lines from the latter reaction were more easily resolved, and the energies of these lines could be measured more accurately. Actually, most of the Ge(Li) singles spectra

TABLE I. α-particle threshold energies for the production of Na^{22} levels in the $F^{19}(\alpha,n)Na^{22}$ reaction.

Level No.	Excitation energy (keV)	Threshold energy (MeV)
1	583	3.065
2	657	3.155
3	891	3.438
4	1528	4.210
5	1937	4.704
6	1952	4.723
7	1984	4.762
8	2211	5.036
9	2572	5.473
10	2969	5.954
11	3059	6.063
12	3527	6.630
13	3711	6.852

for $F^{19}+\alpha$ were recorded for the express purpose of studying the lifetimes of the Na^{22} levels by the Doppler-shift attenuation method (DSAM); the excitation energy and branching-ratio information described here was only obtained incidentally.

Gamma-ray spectra from $F^{19}+\alpha$ were recorded with the Ge(Li) detector at $0°$, $90°$, and $166°$ to the beam at 12 α-beam energies between 4.0 and 7.0 MeV. As stated previously most of this data was taken to study Doppler effects; but all of it yielded information on γ-ray energies and branching ratios. Only the $90°$ data yielded γ-ray energies free of Doppler shifts. However, after the Doppler effects were throughly understood (see Sec. V), the $0°$ and $166°$ data also were used to obtain γ-ray energies. Thus, the values presented here for these γ-ray energies are averages of many different measurements.

Alpha-particle threshold energies for the $F^{19}(\alpha,n)$-Na^{22} reaction are listed in Table I. We found that γ rays from a given Na^{22} level could not be seen in the Ge(Li) singles spectra unless the α energy was $\gtrsim 500$ keV above threshold for production of the level. For instance, no Na^{22} states above the 3.059-MeV level were populated to any observable extent in this work ($E_\alpha \leqslant 7.0$ MeV); population of the 1.528-MeV level was not observed for $E_\alpha \leqslant 4.6$ MeV; and the 2.210-MeV level was not populated to any observable extent for $E_\alpha < 5.4$ MeV. Portions of typical $F^{19}+\alpha$ spectra are shown in Figs. 2 and 3. The Na^{22} γ rays observed in this work are listed in Table II which gives the measured transition energies and assignments.

Both internal and external calibration lines were used in the energy measurements. The internal energy standards were the $F^{19}(\alpha,\alpha'\gamma)F^{19}$ γ rays of 109.87 ± 0.04 and 198 ± 1 keV,[16] annihilation radiation (511.006 ±0.005 keV),[17] and the Ne^{22} $1.275\rightarrow 0$ γ ray (1274.52 ±0.07 keV).[18] External calibration lines used were from radioactive Na^{22} and ThC'' sources. The former emits

[16] F. Ajzenberg-Selove and T. Lauritsen, Nucl. Phys. 11, 1 (1959).
[17] Electron rest mass.
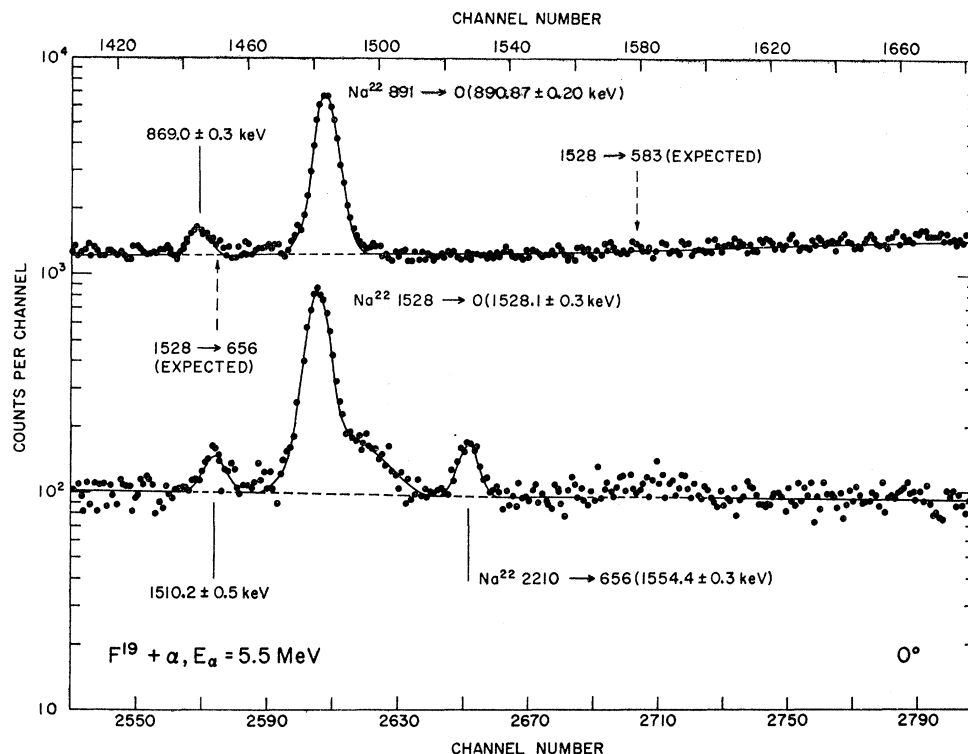[18] W. W. Black and R. L. Heath, Nucl. Phys. A90, 650 (1967).

FIG. 2. Portions of a 4096-channel γ-ray spectrum from bombardment of a 1.0-mg/cm² CaF₂ target with 5.5-MeV α particles. The scales at the top and bottom are for the upper and lower spectra, respectively. The 8-cc Ge(Li) detector was at 0° to the beam and 10 cm from the target. The energy dispersion is 0.567 keV/channel and the energy resolution is ∼3.5-keV FWHM. Three full-energy-loss peaks corresponding to γ-ray transitions in Na²² are identified by the energies (in keV) of the initial and final states between which the transitions take place and by the γ-ray energies. The expected positions of two unobserved Na²² transitions are indicated. Two unidentified γ-ray peaks are also indicated. The solid lines are computer fits to the data points as explained in the text (see Sec. V).

annihilation radiation and the Ne²² $1.275 \rightarrow 0$ γ ray; while the latter emits numerous γ rays, of which those at 238.624 ± 0.009, 583.14 ± 0.023, and 2614.47 ± 0.10 keV[19] were the principal ones used in this work. Some of the γ-ray energies were determined by recording simultaneously γ rays from the Na²² and ThC″ sources and those from F¹⁹+α. For instance, the energies of the γ rays corresponding to the $2.57 \rightarrow 0$ and $2.21 \rightarrow 0.66$ transitions were measured with the full-energy-loss and two-escape peaks of the ThC″ 2.614-MeV γ ray as the principal calibration lines.

The Na²² excitation energies resulting from the γ-ray energies of Table II are given in Table III. Corrections due to the recoil of the Na²² nuclei have been applied in obtaining these excitation energies. The most reliable of the previous energy determinations of the Na²² levels are also listed in Table III. It is seen that the agreement is excellent.

The γ-ray branching ratios of the first 11 excited states of Na²² are given in Table IV. In this table the fifth column summarizes previous work; the sixth column gives the present results and in the seventh column is listed our adopted values obtained by combining the results given in the fifth and sixth columns.

The present results are based on the particle-γ coincidence measurements discussed in Sec. IV as well as the measurements discussed in this section.

Examples of the type of information used to obtain upper limits on particular γ-ray branches are illustrated in Figs. 2 and 3 in which the expected positions of four cascade transitions are indicated by dashed arrows. The upper limits obtained for the relative intensities of the $1.528 \rightarrow 0.583$ and $1.528 \rightarrow 0.657$ transitions (Fig. 2)

TABLE II. γ rays from F¹⁹(α,n)Na²².

E_γ (keV)	Assignment (MeV)
73.9 ±0.1[a]	0.66 → 0.58
583.04±0.1	0.58 → 0
637.50±0.2	1.53 → 0.89
890.87±0.2	0.89 → 0
1016.8 ±0.5	2.97 → 1.95
1107.6 ±0.5	3.06 → 1.95
1280.5 ±1.0	1.94 → 0.66
1368.7 ±0.3	1.95 → 0.58
1400.4 ±0.5	1.98 → 0.58
1527.8 ±0.3	1.53 → 0
1554.4 ±0.3	2.21 → 0.66
1988.8 ±0.4	2.57 → 0.58
2571.2 ±0.3	2.57 → 0

[a] From Ref. 11. Note that the Na²² excitation energies given in the figures are based on a value of 73.0 keV for the energy of this γ ray.

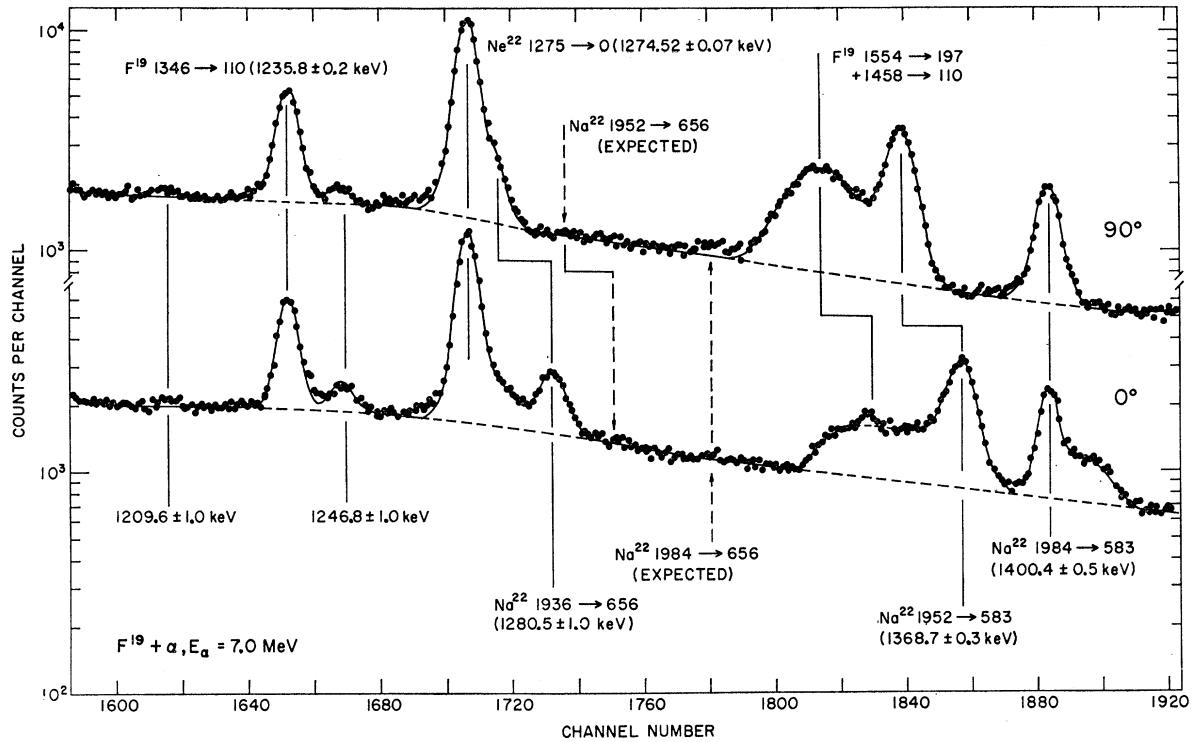[19] G. Murray, R. L. Graham, and J. S. Geiger, Nucl. Phys. 63, 353 (1965).

Fig. 3. Portions of two 4096-channel γ-ray spectra from bombardment of a 1.0-mg/cm² CaF₂ target with 7.0-MeV α particles. The 8-cc Ge(Li) detector was 10 cm from the target and at 0° (lower curve) and 90° (upper curve) to the beam. The energy dispersion is 0.712 keV/channel and the energy resolution is ~4.0-keV FWHM. Full-energy-loss peaks corresponding to γ-ray transitions in F¹⁹ and Na²² are identified by the energies (in keV) of the initial and final states between which the transitions take place and, in most cases, by the γ-ray energies. The expected positions of two unobserved Na²² transitions are indicated as are two unidentified γ-ray peaks. The solid lines are computer fits to the data points as explained in the text (Sec. V).

were considerably less stringent than those obtained from the NaI(Tl)-NaI(Tl) coincidence measurements. On the other hand, the limits given in Table IV for the unobserved 1.952 → 0.657 and 1.984 → 0.657 transitions were obtained from Ge(Li) data such as that of Fig. 3, since the NaI(Tl) energy resolution was not sufficient to resolve these transitions from the observed decays to the 0.583-MeV level.

TABLE III. Excitation energies of the low-lying levels of Na²².

Level	Present work (keV)	Previous work[a] (keV)
1	583.05±0.1	583.0±0.5[b]
2	657.0 ±0.14	656.9±0.5[b,c]
3	890.89±0.2	889 ±5
4	1528.1 ±0.3	1528 ±5
5	1936.9 ±0.23[d]	1933 ±7
6	1951.8 ±0.3	1946 ±7
7	1983.5 ±0.5	1980 ±7
8	2211.4 ±0.32	2211 ±7
9	2571.5 ±0.3	2566 ±7
10	2968.6 ±0.6	2966 ±7
11	3059.4 ±0.6	3058 ±7

a Except for the first two levels these are from Ref. 6.
b Reference 23.
c Assuming an energy of 73.9±0.1 keV for the 0.657 → 0.583 γ ray (Ref. 11).
d Reference 11. Based on an energy of 1279.9±0.2 keV for the 1.94 → 0.66 transition. For this γ ray the present work gave an energy of 1280.5±1.0 keV.

The γ-ray peaks labeled only by their energies in Figs. 2 and 3 were not identified; they do not correspond in energy with possible transitions between any of the known levels of Na²² formed in this study. They may result from Ca+α reactions. The spectra of Figs. 2 and 3 will be discussed further in Sec. V where the Doppler effects evident in these figures will be used to extract lifetimes or lifetime limits for the levels in question.

III. γ-RAY ANGULAR DISTRIBUTIONS

Ge(Li) angular distribution studies of γ rays from the F¹⁹($\alpha,n\gamma$)Na²² reaction were undertaken, in part, to supplement the Ne²⁰(He³,$p\gamma$)Na²² p-γ angular correlation measurements reported in the next section. This was done since it was found in these latter studies that the resolution of neither the surface-barrier proton detector nor the NaI(Tl) γ detector was adequate to resolve the γ-ray transitions from the Na²² 1.952- and 1.984-MeV levels. The excellent resolution of the Ge(Li) detector used in the present angular distribution studies enabled us to easily separate, in particular, those γ rays corresponding to the 1.952 → 0.583 and 1.984 → 0.583 transitions in Na²². Because the low energy of the outgoing neutrons (unobserved) would be expected to emphasize $l_n=0$ partial waves, one could also expect to

TABLE IV. γ-ray branching ratios for the low-lying levels of Na[22].

Level No.	E_i (MeV)	E_f (MeV)	E_γ (keV)	Previous[a]	Present	Adopted
2	0.657	0.583	73.9	100	100	100
3	0.891	0	890.9	100	100	100
		0.583	307.8	...	<0.5	<0.5
		0.657	233.9	...	<0.3	<0.3
4	1.528	0	1528.1	>95	95.5±1.2	95.5±1.2
		0.583	945.0		<0.5	<0.5
		0.657	871.1	<5	<0.5	<0.5
		0.891	637.2		4.5±1.2	4.5±1.2
5	1.937	0	1936.9	<3	<2	<2
		0.583	1353.9	<3	<7	<3
		0.657	1279.9	100	100	100
		0.891	1046.0	<4	<5	<4
		1.528	408.8	<2	<2	<2
6	1.952	0	1951.8	...	<2	<2
		0.583	1368.8		100	100
		0.657	1294.8	100	<3	<3
		0.891	1060.9	...	<0.5	<0.5
		1.528	423.7	...	<0.5	<0.5
7	1.984	0	1983.5	...	<2	<2
		0.583	1400.5		100	100
		0.657	1326.5	100	<3	<3
		0.891	1092.6	...	<5	<5
		1.528	455.4	...	<4	<4
8	2.211	0	2211.4	...	1±1	1±1
		0.583	1628.4	...	<3	<3
		0.657	1554.4	100	99±1	99±1
		0.891	1320.5	...	<1.6	<1.6
		1.528	683.3	...	<1	<1
9	2.572	0	2571.5	81±4	82±5	81±3
		0.583	1988.5	19±4	18±5	19±3
		0.657	1914.5	...	<5	<5
		0.891	1680.6	<2	<4	<2
		1.528	1043.4	<2	<6	<2
		1.937	634.6	<4	...	<4
		1.952	619.7	<4	<7	<4
		1.984	588.0	<4	<30	<4
		2.211	360.1	<10	<7	<7
10	2.969	0	2968.6	<1	<7	<1
		0.583	2385.6	<1	<3	<1
		0.657	2311.6	<1	<3	<1
		0.891	2077.7	<1	<2	<1
		1.528	1440.5	<2	<4	<2
		1.937	1031.7	...	<0.7	<0.7
		1.952	1016.8	100	100	100
		1.984	985.1	...	<6	<6
		2.211	757.2	<2	<6	<2
		2.572	397.1	<2	<6	<2
11	3.059	0	3059.4	<1	<25	<1
		0.583	2476.4	3±1	<15	3±1
		0.657	2402.4	<1	<10	<1
		0.891	2168.5	<2	<20	<2
		1.528	1531.3	<3	...	<3
		1.937	1122.5	<20	<2	<2
		1.952	1107.6	97±1	100	97±1
		1.984	1075.9	...	<16	<16
		2.211	848.0	<4	...	<4
		2.572	487.9	<3	<15	<3

[a] The results for levels 2, 3, 4, 6, 7, and 8 are from Ref. 2. Those for level 5 are from Ref. 11, those for level 9 are from Refs. 2 and 12, and those for levels 10 and 11 are from Ref. 12.

obtain significant nuclear alignments through the $F^{19}(\alpha,n\gamma)Na^{22}$ reaction.

Angular distributions were measured by recording Ge(Li) γ-ray spectra for a known integrated beam current for detection angles θ_γ relative to the beam direction of 0°, 30°, 45°, 60°, and 90° at an α-beam energy of 5.48 MeV. The 0° and 90° spectra were similar to those shown in Fig. 3; the main difference being that the relative intensities of the two unresolved γ rays corresponding to the F^{19} $1.554 \rightarrow 0.198$ and $1.458 \rightarrow 0.110$ transitions were considerably reduced for the $E_\alpha = 5.48$-MeV spectra.
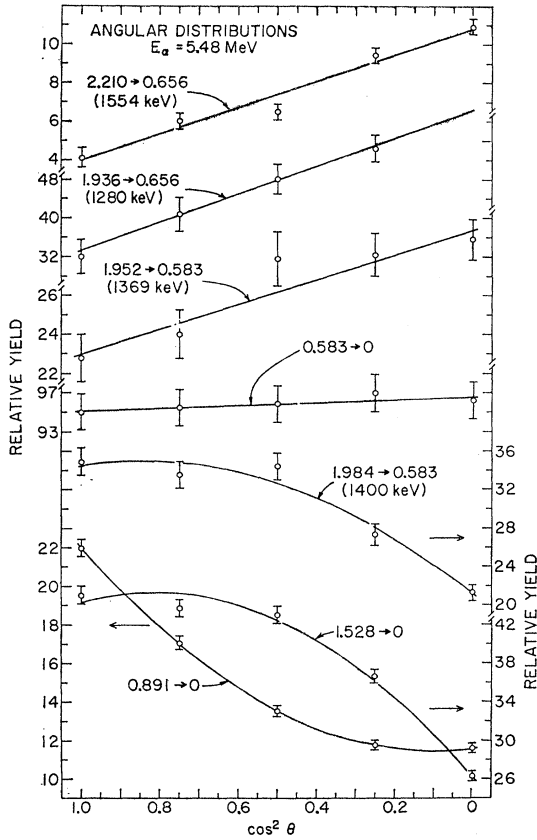
FIG. 4. Angular distributions of Na^{22} γ rays obtained from $F^{19}(\alpha,n\gamma)Na^{22}$ with $E_\alpha=5.48$ MeV and a 1.0-mg/cm² CaF₂ target. An 8-cc Ge(Li) γ-ray detector at 10 cm from the target was used to record the γ-ray spectra. The full curves are least-squares fits to the function $W(\theta)=A_0+A_2P_2(\cos\theta)+A_4P_4(\cos\theta)$. The γ rays are identified by the energies (in MeV) of the initial and final states between which the transitions take place, and, in the case of cascade transitions, by the γ-ray energies in keV.

The angular distributions extracted from these spectra are shown in Fig. 4 together with least-squares fits to the Legendre-polynomial expansion:

$$W(\theta)=A_0+A_2P_2(\cos\theta)+A_4P_4(\cos\theta).$$

The expansion coefficients A_2/A_0 and A_4/A_0 are listed in Table V.

The angular distributions summarized in Table V are quite similar to those obtained for the same transitions in the p-γ angular correlation work (see Sec. IV). This is consistent with the nuclear alignment being similar in the two cases, which in turn, is consistent with the hypothesis that $l_n=0$ partial waves dominate the neutron angular distributions in the $F^{19}(\alpha,n)Na^{22}$ reaction at $E_\alpha=5.48$ MeV: for if $l_n=0$ neutrons are emitted then only magnetic substates α of the residual levels in Na^{22} with values of 0 or ±1 are populated in this reaction. This is the same constraint as that imposed by the collinear geometry[20] used in the $Ne^{20}(He^3,p\gamma)Na^{22}$ angular correlation measurements.

[20] A. E. Litherland and A. J. Ferguson, Can. J. Phys. **39**, 788 (1961).

From Table V we see that the $1.984\to0.583$ transition has a significant $P_4(\cos\theta)$ term and the $1.952\to0.583$ transition has a significant $P_2(\cos\theta)$ term. This means that the Na^{22} 1.984-MeV level has $J\geqslant2$ and the 1.952-MeV level has $J\geqslant1$. This is the most important information obtained from these angular distribution measurements.

IV. PROTON-γ ANGULAR CORRELATIONS

A. Experimental Procedures

Proton-γ correlations in the $Ne^{20}(He^3,p\gamma)Na^{22}$ reaction were studied at a He^3 bombarding energy of 5.65 MeV. The enriched Ne^{20} gas[13] was contained in a cylindrical gas cell 0.6 cm long at a pressure of $\frac{1}{3}$ atm. The cell axis was coincident with the beam axis. The ends of the cell were of 0.05-mil nickel foil. Protons were detected by an annular solid-state detector, which was centered at 180° to the beam direction and 4 cm from the target, subtending an angle θ_p of $(171\pm1.7)°$ at the target center. The beam passed through a hole in the center of the annular detector, through the gas cell, and was stopped in a 1-mil Mo foil at the rear of the scattering chamber. The scattering chamber was somewhat different from that previously used at this laboratory,[21] the main difference being a considerable reduction in material (in the region $0°\leqslant\theta_\gamma\leqslant90°$), with a corresponding reduction in the absorption of γ rays. This chamber is described elsewhere.[22]

The annular detector viewed charged particles emanating from the entrance and exit nickel foils as well as from the gas volume. He^3 particles scattered from these foils as well as those scattered from the gas were prevented from reaching the detector by an aluminum absorber foil of 1.2-mil thickness; all α-particle groups from the $Ne^{20}(He^3,\alpha)Ne^{19}$ reaction were also stopped by this absorber. Gamma rays were detected by a 3×3-in. NaI(Tl) crystal placed with its front face 14.5 cm from the target volume. The spectrum of coincidence pulses from the two detectors was analyzed by the TMC 16 384-channel two-parameter

TABLE V. Summary of results for $F^{19}(\alpha,n\gamma)Na^{22}$ angular distributions at $E_\alpha=5.48$ MeV.

γ ray (MeV)	Transition (MeV)	A_2/A_0[a]	A_4/A_0[a]
0.583	$0.583\to0$	$-(0.01\pm0.02)$	$-(0.01\pm0.02)$
0.891	$0.891\to0$	$+(0.43\pm0.02)$	$+(0.22\pm0.03)$
1.275	$1.275\to0(Ne^{22})$	$+(0.16\pm0.03)$	$-(0.05\pm0.03)$
1.280	$1.937\to0.657$	$-(0.34\pm0.07)$	$-(0.04\pm0.05)$
1.369	$1.952\to0.583$	$-(0.14\pm0.04)$	$-(0.04\pm0.04)$
1.400	$1.984\to0.583$	$+(0.38\pm0.04)$	$-(0.15\pm0.04)$
1.528	$1.528\to0$	$+(0.41\pm0.02)$	$-(0.18\pm0.02)$
1.554	$2.211\to0.657$	$-(0.55\pm0.05)$	$-(0.05\pm0.05)$

[a] The quoted values of A_2/A_0 and A_4/A_0 have been corrected for the finite solid angle subtended by the Ge(Li) detector.

[21] J. W. Olness and E. K. Warburton, Phys. Rev. **151**, 792 (1966).

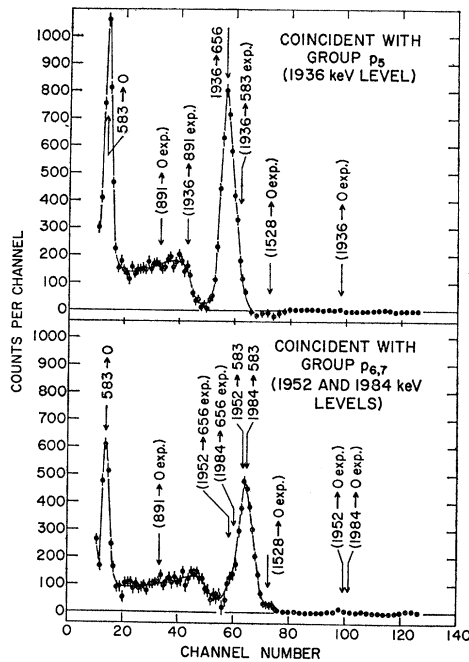[22] A. R. Poletti, Phys. Rev. **153**, 1108 (1967).

FIG. 5. Partial results of a two-parameter analysis of p-γ coincidences from the $Ne^{20}(He^3,p\gamma)Na^{22}$ reaction at a bombarding energy $E_{He^3}=5.65$ MeV. The plot shows the proton spectrum measured in coincidence with all γ-ray pulses of energy $E_\gamma>550$ keV. The data are the sum of 10 spectra recorded at 5 different angles θ_γ. The proton peaks are identified by the excitation energies (in keV) of the Na^{22} levels to which they correspond. Partial decomposition of the 1.95-MeV triplet is illustrated in the insert.

analyzer operating in a 128×128-channel mode. Data were acquired for γ-ray detection angles $\theta_\gamma=0°$, $30°$, $45°$, $60°$, and $90°$ in random order. This sequence was then repeated as a check on reproducibility. Thus 10 separate two-dimensional spectra were recorded with an average duration of 4 h. The beam current was 90 nA and the coincidence resolving time was ~70 nsec. The results of each experimental measurement were transcribed onto magnetic tape for later computer analyses; at the conclusion of the correlation measurements the individual spectra corresponding to the various θ_γ were added to form a "summed spectrum," which was used to determine decay schemes. Corrections due to correlation effects were later determined, from the results of the correlation analysis, to be small; they were nevertheless applied in the final determination of branching ratios. These procedures were described in more detail previously.[21]

The different spectra were normalized to the integrated beam charge. As a check on this normalization procedure an electronic gate was set to select the region of the proton singles spectra which included the two most prominent proton groups of Fig. 5. The ratio of these proton monitor counts to the integrated charge was constant to within 4% for the 10 recorded spectra.

B. Results

γ-Ray Spectra

Partial results of analyses of the "summed spectrum" are shown in Figs. 5, 6, and 7. Figure 5 shows protons in

coincidence with γ-ray pulses corresponding to $E_\gamma>550$ keV. The insert shows separation of the 1.95-MeV triplet into two proton groups accomplished by utilizing the separation in the γ-ray detector of the 1.28-MeV $1.94\rightarrow0.66$ transition from the unresolved $1.95\rightarrow0.58$ and $1.98\rightarrow0.58$ transitions. Randoms, which amounted to 20% of the total counts, have been subtracted from this and all other spectra. The two-dimensional random spectra were generated from proton and γ-ray singles spectra.[21]

In Figs. 6 and 7 are shown γ-ray spectra in coincidence with the indicated proton groups. The spectra of Fig. 6 were obtained in a straightforward manner; however, the extraction of the spectra shown in Fig. 7 demanded a careful separation of contributions from the individual unresolved proton groups. The spectrum shown for the 1.937-MeV level was obtained, for example, by subtracting a fraction of the γ-ray spectrum observed in coincidence with a group of channels on the upper side of the unresolved 1.9-MeV triplet from the γ-ray spectrum observed in coincidence with a group of proton channels on the lower side. The spectrum due to the unresolved 1.952- and 1.984-MeV levels was obtained in a similar fashion. The appropriate fraction was determined for each case from the data shown in the insert of Fig. 5.

In Figs. 6 and 7 we have indicated, in addition to the prominent γ-ray peaks, the expected peak positions of

FIG. 6. Spectra of γ rays from the $Ne^{20}(He^3,p\gamma)Na^{22}$ reaction measured in coincidence with proton groups p_4 and p_8 populating, respectively, the 1.528- and 2.211-MeV levels of Na^{22}. For each spectrum the γ-ray peaks are identified by the energies (in keV) of the initial and final states between which the transitions occur. The expected positions of some unobserved peaks are also indicated.

FIG. 7. Spectra of γ rays from the $Ne^{20}(He^3,p\gamma)Na^{22}$ reaction measured in coincidence with proton groups p_5 and $p_{6,7}$ (unresolved) populating, respectively, the 1.937-MeV level and the 1.952- and 1.984-MeV levels of Na^{22}. For each spectrum the γ-ray peaks are identified by the energies (in keV) of the initial and final states between which the transitions occur. The expected positions of some unobserved peaks are also indicated. These spectra were obtained from the two-parameter "summed spectrum" by unfolding the contributions due to the unresolved triplet of proton groups as is explained in the text.

various other possible transitions. From these data, branching ratios (or upper limits) were determined for the 1.528-, 1.937-, 1.984-, and 2.211-MeV levels; the relative population of the 1.952-MeV level was too weak for an accurate determination of its de-excitation. The resultant information concerning γ-ray branching ratios has been incorporated into Table IV.

γ-Ray Angular Correlations

The 10 individual p-γ coincidence spectra were analyzed routinely using the procedures outlined above for the "summed spectra." By this means angular correlations were extracted for 5 γ-ray peaks, one of which consisted of the unresolved $1.984 \rightarrow 0.583$, $1.952 \rightarrow 0.583$ doublet. A sixth γ-ray transition observed in the two-dimensional spectra, the $1.528 \rightarrow 0.891$ transition, was too weak in intensity for a meaningful correlation to be extracted. The correlations involving the 0.583-MeV γ ray were not analyzed because the mean lifetime of the 0.583-MeV level is 351 ± 3 nsec[23] which was ~5 times the resolving time of the coincidence unit.

For each angle θ_γ there were two separate measurements of the normalized counting rates. These provided

[23] A. W. Sunyar and P. Thieberger, Phys. Rev. **151**, 910 (1966).

(with one exception) a satisfactory check on the internal consistency of the measurements. The data points were therefore averaged and the resulting correlations were fitted by the method of least-squares to yield the Legendre polynomial coefficients listed in Table VI. The exception is for transitions originating from the 1.528-MeV level; the results indicating that the final three correlation points were low by $\sim10\%$. This observation could be explained by a small change in the He^3 bombarding energy (~20 keV) after the seventh point was recorded since the relative yield to the 1.528-MeV level was observed to exhibit a resonance behavior and the He^3 energy had been chosen to maximize this yield. Only the first five spectra were used in the analysis of the $1.528 \rightarrow 0$ angular correlation. For the other Na^{22} levels analyzed, there was no evidence of resonance behavior in proton singles spectra, nor was there evidence for any effects due to the (possible) ~20-keV change in the He^3 energy.

For three of the transitions listed in Table VI, the coefficients A_2/A_0 and A_4/A_0 are listed since the fit was to

$$W(\theta) = A_0 + A_2 P_2(\cos\theta) + A_4 P_4(\cos\theta).$$

For the $1.937 \rightarrow 0.657$ and $2.211 \rightarrow 0.657$ transitions, only A_2/A_0 is listed since the fit was to

$$W(\theta) = A_0 + A_2 P_2(\cos\theta).$$

The latter fits were restricted because previous work,[2,11] confirmed by the present results, demand $J=1$ for the 1.937- and 2.211-MeV levels (see Fig. 1).

The values of X^2 listed in Table VI have been normalized to the degrees of freedom and thus have expectation values of unity.[24] In a preliminary analysis, in which only statistical errors were included, it was found that X^2 tended to be large compared to unity. This indicated that the statistical uncertainties assigned to the correlations should be increased to account also for possible systematic errors. (One possible source of systematic errors has been discussed with reference to the results for the $1.528 \rightarrow 0$ distribution.) Systematic errors were estimated by demanding that the external and internal errors of the least-squares fits to *all* the correlations of Table VI, considered as a group, be equal. The systematic errors so obtained were, on the average, comparable to the statistical errors.

The method of analysis of particle-γ angular correlations measured in a collinear geometry[20] has become quite standard; we use specifically that presented by Poletti and Warburton.[24] Briefly, the method relies on the fact that only the $\alpha=0$ and ±1 magnetic substates of a Na^{22} level can be formed in the $Ne^{20}(He^3,p)Na^{22}$ reaction if the protons are detected along the beam axis, i.e., $\theta_p=0°$ or $180°$. The effect of small departures from this condition, i.e., $\theta_p=(171\pm1.7)°$ in the present measurements, allows some population of higher substates.

[24] A. R. Poletti and E. K. Warburton, Phys. Rev. **137**, B595 (1965).

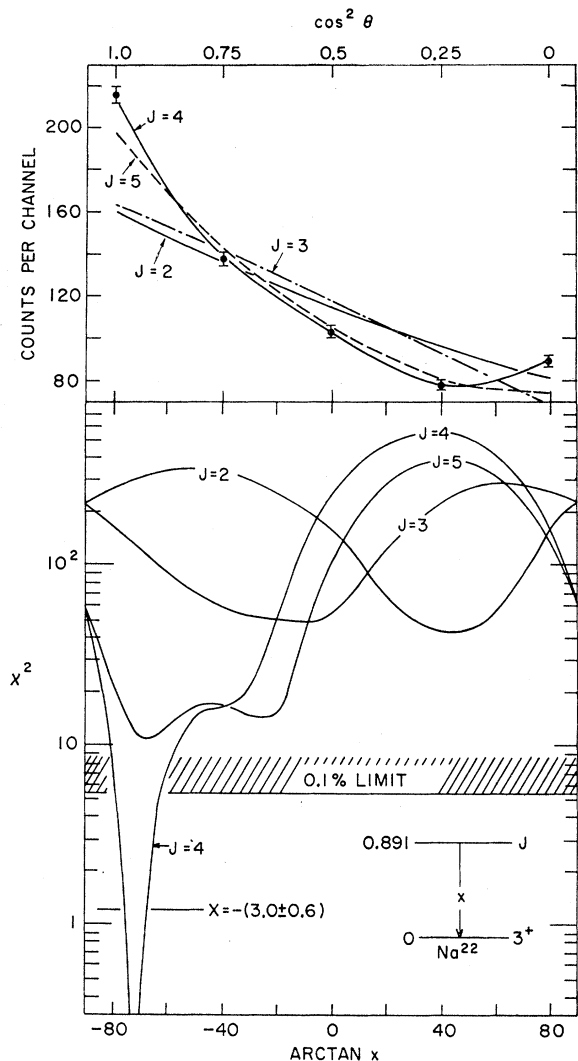FIG. 8. Proton-γ angular correlation for the Na[22] $0.891 \to 0$ transition resulting from population of the 0.891-MeV level in the Ne[20](He[3],p)Na[22] reaction. The points with error bars (upper plot) show the experimental correlation data. The results of a χ^2-analysis of these data are shown in the lower part of the figure. Here we have plotted χ^2, representing the goodness-of-fit to the experimental data, as a function of arctan$x$, where x is the $(L+1)/L$ mixing ratio in the $0.891 \to 0$ transition. For a correct solution the expectation value of χ^2 is unity and the probability of χ^2 exceeding the 0.1% limit is 0.1%. Plots are shown for assumed values of $J=2$ through 5 for the 0.891-MeV level. The FSE (see text) is unimportant for these plots. It is seen that only $J=4$ with a quadrupole/dipole mixing ratio of $x=-(3.0\pm0.6)$ gives an acceptable solution. The best fit for each assumed value of J is shown in the upper part of the figure.

The maximum likely extent of this effect, termed the finite-size effect (FSE) can be easily estimated.[20,24] In the present work it was usually found to be negligible.

The analysis proceeds as follows: Spins are assumed for the initial and final states of the transition and the transition is assumed to be a mixture of the lowest and next-to-lowest allowed multipolarities. Then a value of the ratio x of the amplitudes of these two multi-
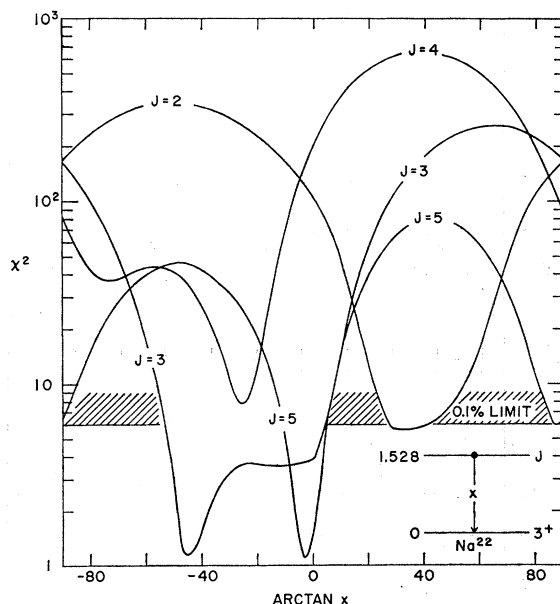
FIG. 9. Proton-γ angular correlation results for the Na[22] $1.528 \to 0$ transition. For details see the caption of Fig. 8 and the text. These results eliminate spins of $J=2$ and 4 for the Na[22] 1.528-MeV level.

polarities is assumed and a least-squares fit is made to the angular correlation, the only unknown being the ratio $P(1)/P(0)$ of the populations of the two possible magnetic substates of the initial state. This procedure is repeated for different values of x until a χ^2-versus-arctan$x$ curve is generated for a particular set of initial and final spins. This procedure is then repeated for all possible spin sets. The sign convention used for x is that of Litherland and Ferguson[20] and of Poletti and Warburton[24] for ML, $EL+1$ mixtures. It is the same as that recently recommended by Rose and Brink.[25]

The results of this procedure are shown in Figs. 8 and 9 for the $0.891 \to 0$ and $1.528 \to 0$ transitions, respectively. The lower curve in Fig. 8 shows the χ^2-versus-arctan$x$ curves just discussed, while the upper curve shows the experimental angular distribution and the best fitting theoretical distribution for each spin set.

From Fig. 8 it is apparent that the Na[22] 0.891-MeV level has $J=4$ and a quadrupole-dipole mixing ratio of $x=-(3.0\pm0.6)$. This result is in fair agreement with the earlier work of Carola[8] who found $J=4$ and $x=-(1.7\pm0.9)$. The average of these two determinations of x, $-(2.6\pm0.5)$, is in the region allowed by both experiments and we adopt it for later discussion.

From Fig. 9 we see that three values of J, the spin of the Na[22] 1.528-MeV level, give χ^2 curves which drop below the 0.1% limit, our criterion for allowed solutions. This was also found to be the case in the previous study of Ne[20](He[3],$p\gamma$)Na[22] angular correlations.[2] However, in both cases $J=2$ was ruled against with a con-

---

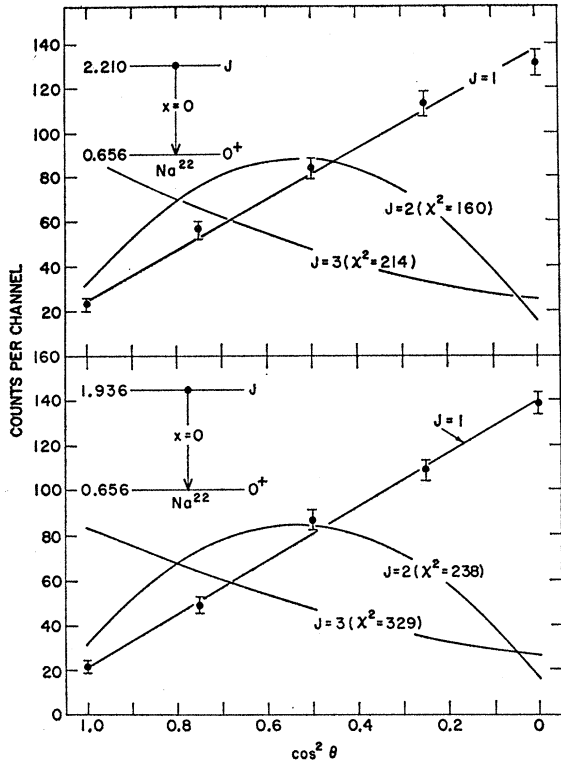[25] H. J. Rose and D. M. Brink, Rev. Mod. Phys. **39**, 306 (1967).

FIG. 10. Proton-γ angular correlation results for the Na^{22} 1.937 → 0.657 transition (lower curve) and 2.211 → 0.657 transition (upper curve). The data points show the experimental data while the curves show the best fits to the data obtained, as indicated in the inserts, for assumed spins of $J=1, 2$, and 3 for the initial state of the transition. For the $J=2$ and 3 assumptions the minimum value of χ^2 is indicated. The uncertainties have been adjusted so that $\chi^2=1$ for $J=1$. The assignments $J=2$ and 3 are excluded by these results for both levels.

fidence of 99% and so the two experiments together quite definitely rule out $J=2$. For $J=3$, we find an acceptable solution for a quadrupole-dipole mixing ratio of $x=-(1.05\pm0.15)$. This is to be compared to the value $x=-(1.36\pm0.18)$ obtained by Maier et al.[2] A value of $-(1.18\pm0.15)$ is allowed by both experiments and we adopt it for later discussion.

For $J=5$, we find that an octupole-quadrupole mixing ratio of $x=-(0.04+0.05)$ gives an acceptable solution. It will be shown in the next section that this transition cannot contain a significant octupole component, i.e., x may differ only negligibly from 0. The present result is consistent with this restriction. Maier et al.[2] also found that $J=5$ and $x=0$ gave an acceptable solution.

Since the Na^{22} 0.657-MeV level has $J^\pi=0^+$, the 2.211 → 0.657 and 1.937 → 0.657 transitions are pure multipoles, i.e., $x=0$. The best fitting theoretical correlations for these two cases are shown in Fig. 10 for assumed spins of $J=1, 2$, and 3 for the initial state. It is clear that $J=1$ for both the 1.937- and 2.211-MeV levels, in agreement with previous results.[2,11]

Some difficulty was encountered in extracting from the data the angular correlation of the 1.984 → 0.583

transition, since the proton detector was incapable of resolving the proton groups leading to the 1.984- and 1.952-MeV levels (see inset of Fig. 5), while the γ-ray detector was similarly incapable of resolving the 1.400- and 1.369-MeV γ rays de-exciting these states (see Fig. 7). No difficulty was encountered in extracting the 1.937 → 0.657 correlation, since the 1.280-MeV γ ray was well-resolved from the (1.400+1.369)-MeV doublet γ rays. With respect to the data shown in the inset of Fig. 5, we note that the centroid of the (1.984+1.952)-MeV doublet peak corresponds more closely to the peak position calculated (relative to the 1.937-MeV peak) for the 1.984-MeV peak. From these data, and from similar considerations on the (1.400+1.369) doublet γ-ray peaks, we deduce the following relative populations for the 1.9-MeV triplet levels: 1.984:1.952:1.937::5:1:6.

In Table VI we have summarized the results of a Legendre polynomial fit to the angular correlation of unresolved (1.400 and 1.369)-MeV γ rays from the 1.984- and 1.952-MeV levels. Since the relative population of the 1.952-MeV level is only ~20% that of the 1.984-MeV level, we expect that the measured correlation is dominated by the 1.984 → 0.583 correlation effects. In order to see this more clearly, we obtained from the two-parameter data for each angle θ_γ the proton spectrum in coincidence with the 1.400- and 1.369-MeV photopeaks. The resultant spectra, similar to the insert of Fig. 5, were then fitted with a Legendre polynomial expression to obtain plots of A_0, A_2, and A_4 as a function of proton channel number. It was thus clear that the large A_4 coefficient is associated with the 1.984 → 0.583 transition, since it peaks at the channel number corresponding to proton group p_7 (1.984-MeV level); these results are further consistent with $A_4=0$ for the 1.952 → 0.583 transition. From the plots of A_0 and A_2 versus channel number it was also possible to estimate and subsequently remove the 1.952 → 0.583 contribution to the unresolved doublet correlation. The resultant data on the 1.984 → 0.583 transition were then fitted to yield the Legendre-polynomial coefficients $A_2/A_0=+(0.35\pm0.06)$ and $A_4/A_0=-(0.36\pm0.06)$.

Figure 11 shows the results of a χ^2 analysis of the 1.984 → 0.583 correlation data for assumed spins $J=3$ and $J=2$ for the 1.984-MeV level. Possibilities $J<2$ are removed by the observation of a nonzero A_4 coeffi-

TABLE VI. Results of least-squares Legendre-polynomial fits to proton-γ angular correlations measured in the $Ne^{20}(He^3,p\gamma)Na^{22}$ reaction.

Transition (MeV)	A_2/A_0[a]	A_4/A_0[a]	χ^2
0.891 → 0	+(0.62±0.05)	+(0.60±0.05)	0.10
1.528 → 0	+(0.55±0.06)	−(0.23±0.07)	0.98
1.937 → 0.657	−(0.82±0.04)	⋯	0.88
1.984 → 0.583 1.952 → 0.583	+(0.38±0.05)	−(0.30±0.05)	2.10
2.211 → 0.657	−(0.77±0.03)	⋯	1.44

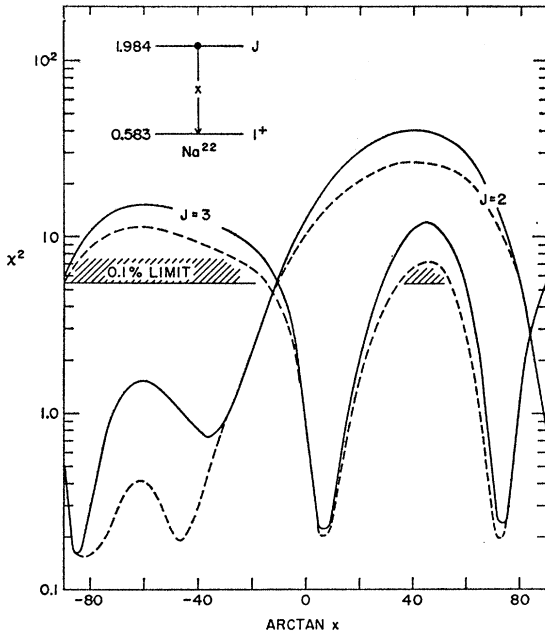[a] These values include a correction for the finite solid angle subtended by the NaI(Tl) detector.

FIG. 11. Results of a χ^2 analysis of p-γ correlations, measured in the $Ne^{20}(He^3,p\gamma)Na^{22}$ reaction, for the Na^{22} 1.984-MeV level. Here χ^2 is plotted as a function of x, the $(L+1)/L$ mixing parameter in the $1.984 \rightarrow 0.583$ transition, for assumed spins for the 1.984-MeV level of $J=2$ and $J=3$. (Possible assignments $J \leqslant 1$ and $J > 3$ have been previously rejected, as explained in the text.) From these results we see that for particular values of x both of these possible spin assignments are acceptable. The dashed curves show our estimate of the maximum possible effect (FSE) of the finite size of the annular particle detector.

cient (see Tables V and VI), while possible assignments $J > 3$ are not allowed by the lifetime of this level (see Sec. V). From Fig. 11 we see that, on the basis of the present data alone, either assignment $J=2$ or $J=3$ is allowed. For $J=2$ the quadrupole/dipole mixing is restricted to values $x < -0.20$ or $x > 5$. For $J=3$, solutions for the octupole/quadrupole mixing ratio are $x=+(0.12_{-0.15}^{+0.20})$ or $x=+(3.4_{-1.4}^{+2.4})$. Only the first solution for $J=3$ is consistent with the restriction imposed by the lifetime of the 1.984-MeV level, discussed in the following section, that $x \simeq 0$ for $J=3$.

V. LIFETIME MEASUREMENTS

A. The Doppler-Shift Attenuation Method (DSAM)

Study of the Doppler effects associated with the emission of γ radiation from nuclei recoiling in matter has become a widely used method of obtaining information on the lifetimes of nuclear levels.[21,26–29] In this subsection we shall outline the methods used to extract values or limits for the mean lifetimes of the Na^{22} levels under consideration. The analysis is an extension of methods used previously at this laboratory.[21,27,28]

[26] A. E. Litherland, M. J. L. Yates, B. M. Hinds, and D. Eccleshall, Nucl. Phys. 44, 220 (1963).

[27] E. K. Warburton, D. E. Alburger, and D. H. Wilkinson, Phys. Rev. 129, 2180 (1963).

[28] E. K. Warburton, J. W. Olness, K. W. Jones, C. Chasman, R. A. Ristinen, and D. H. Wilkinson, Phys. Rev. 148, 1072 (1966).

[29] P. Paul, J. B. Thomas, and S. S. Hanna, Phys. Rev. 147, 774 (1966).

With the $F^{19}(\alpha,n)Na^{22}$ reaction and α energies not too far from the threshold for production of a given excited state of Na^{22*}, the energy of the recoiling Na^{22*} nuclei is fairly well defined and the direction of motion of these nuclei is confined to a fairly narrow cone centered about the z axis (beam axis). We shall first assume that the Na^{22*} recoils are monoenergetic and are all emitted along the z axis. The validity of this assumption and the uncertainties associated with it are discussed in Appendix A. These uncertainties are taken into account in the final analysis.

The average energy $\bar{E}_\gamma$ of the γ radiation emitted from an ensemble of nuclei formed at $t=0$ with initial velocity along the z axis and moving thereafter with speed $v(t)$, or $c\beta(t)$, can be expressed as

$$\bar{E}_\gamma = E_{\gamma 0}[1 + F(\tau)\beta(0)\cos\theta] \qquad (1)$$

for $\beta(t) \ll 1$. In Eq. (1) $E_{\gamma 0}$ is the γ-ray energy when emitted by a nucleus at rest and θ is the angle of emission of the γ rays relative to the z axis. In general the direction of $\beta(t)$ will differ from that of $\beta(0)$ due to scattering of the recoil nuclei as they are slowed down and stopped in a material. This difference in direction must be incorporated in the definition of $F(\tau)$. We define $\phi(t)$ as the instantaneous angle of $\beta(t)$ to the z axis so that $\beta_z(t) = \beta(t)\cos\phi(t)$, and $\beta_z(0) \equiv \beta(0)$. In Eq. (1), $F(\tau)$ is an attenuation coefficient which lies between 0 and 1 and can be expressed as[30]

$$F(\tau) = \frac{1}{\tau\beta(0)} \int_0^\infty \beta_z(t)e^{-t/\tau}dt. \qquad (2)$$

The lifetime of the γ-emitting level in question can be determined if $F(\tau)$ differs measurably from 0 and 1; otherwise a limit can be obtained for the mean lifetime. We have obtained values of $F(\tau)$ from the observed energy shift with γ-ray detector angle of the Na^{22} γ-ray lines. That is, from Eq. (1) we have,

$$F(\tau) = \frac{\Delta E_\gamma}{E_{\gamma 0}\beta(0)(\cos\theta_1 - \cos\theta_2)}, \qquad (3)$$

where $\Delta E_\gamma = \bar{E}_\gamma(\theta_1) - \bar{E}_\gamma(\theta_2)$ and θ_1 and θ_2 are two different γ-ray detector angles. Note that $E_{\gamma 0}\beta(0)$ is the $0°$–$90°$ Doppler shift expected for lifetimes very short compared to the slowing down process, i.e., for $F(\tau)=1$.

We have also studied the distribution in energy of the γ rays emitted at $0°$ to the beam, i.e., $\theta=0$. For $\theta=0$ there will be a continuous distribution of γ-ray

[30] This treatment is quite similar to one given previously (Refs. 21, 27, and 28), the difference being that the previous treatment assumed no scattering of the recoiling nuclei. i.e., $\cos\phi(t) \cong 1$. The form of Eq. (2) does not of itself imply $F(\tau) \geqslant 0$ and, in fact, if $\cos\phi(t) \neq 1$ the lower limit is not exact; however, deviations from it are expected to be negligible because of the nature of the slowing down and scattering processes. This can be qualitatively understood by noting that the large-angle scattering necessary to produce negative values of $F(\tau)$ is accompanied by large energy losses so that if $\cos\phi(t)$ changes sign then $\beta_z(t)$ becomes almost negligibly small.

energies between $E_{\gamma 0}$ and $E_{\gamma 0}[1+\beta(0)]$ corresponding to a continuous range of the z component of ion velocity between 0 and $\beta(0)$. This distribution, which we designate $dN(V)/dV$, with $V \equiv v_z(t)/v(0) \equiv \beta_z(t)/\beta(0)$, gives the γ-ray line shape once the detector resolution is folded into it. The attenuation coefficient $F(\tau)$ can also be expressed in terms of $dN(V)/dV$:

$$F(\tau) = \int_0^1 V \frac{dN(V)}{dV} dV \bigg/ \int_0^1 \frac{dN(V)}{dV} dV. \qquad (4)$$

We shall assume that the z component of ion velocity is changing with time according to the relation[31]

$$-M_1 dv_z/dt = K_n(v_z/v_0)^{-1} + K_e(v_z/v_0), \qquad (5)$$

where M_1 is the mass of the moving ion and $v_0 = c/137$. The origin of Eq. (5) and its region of validity are discussed in Appendix B. Expressions for the attenuation coefficient $F(\tau)$ and the frequency distribution of γ rays, $dN(V)/dV$, corresponding to a generalization of Eq. (5) are also given in Appendix B and have been discussed previously.[21,27,28] Both $F(\tau)$ and $dN(V)/dV$ can be expressed as functions of two variables, α/τ and γ_i^2, where α is the characteristic slowing-down time of the ions due to electronic processes ($\alpha = M_1 v_0/K_e$), and γ_i^2 depends on the initial velocity of the ions $v(0)$, on the electronic stopping parameter K_e, and on the nuclear stopping and scattering parameter K_n, through the relation $\gamma_i^2 = (K_e/K_n)[v(0)/v_0]^2$. Evaluation of α and γ_i^2 from energy loss and range data are discussed, for Na^{22} ions stopping in CaF_2 and nickel, in Appendix B.

It is obvious from Eq. (4) that the γ-ray line shape, $dN(V)/dV$, contains more information than does $F(\tau)$. We shall show that γ_i^2 and α/τ can be obtained simultaneously from an analysis of the measured $dN(V)/dV$. In contrast γ_i^2 must be assumed in order to extract α/τ from a measurement of $F(\tau)$. Since one of the largest uncertainties we encountered in obtaining the Na^{22} lifetimes from the Doppler-shift data was that associated with inexact knowledge of the nuclear stopping and scattering process, the analysis of the experimental $dN(V)/dV$ results in an increased accuracy for the lifetime determinations and an increased confidence in the method of analysis.

B. Determination of Lifetimes

Determination of $F(\tau)$

For most of the transitions studied here data were acquired at several bombarding energies and angles ($0°$, $90°$, $166°$) in order to determine the experimental Doppler shifts ΔE_γ and subsequently the attenuation factors $F(\tau)$. The energy calibration for this work was based on the positions in these spectra of reference lines of known energy.

Values of ΔE_γ were extracted from this data using computer programs that fitted each region of interest with an assumed functional form for the background and either fitted the peak with a Gaussian or calculated the centroid of the peak. For the peaks yielding limits for $F(\tau)$ the peak centroids were in excellent agreement with the peak positions of the Gaussian. The fits shown in Figs. 2 and 3 are for Gaussian peaks (sometimes unresolved) superimposed on exponential backgrounds. For most transitions this procedure was most straightforward. For the $1.937 \rightarrow 0.657$ transition, which was unresolved from the Ne^{22} $1.275 \rightarrow 0$ transition for $\theta > 60°$, the situation was complicated by the fact that the Ne^{22} $1.275 \rightarrow 0$ transition has a discernible Doppler line shape (see Fig. 3). [A lifetime could not be extracted for the Ne^{22} 1.275-MeV level because it is fed in unknown proportions by (1) direct population in $F^{19}(\alpha,p)Ne^{22}$, (2) γ cascades from higher states, and (3) β decay of Na^{22}.] However, the $F^{19}(\alpha,n\gamma)Na^{22}$ angular distribution data (Sec. III) could be used to obtain the Doppler shift of the Na^{22} $1.937 \rightarrow 0.657$ line, since for $\theta \leqslant 60°$ it was clearly resolved from the Ne^{22} line. A value for the Doppler shift was also obtained by combining the γ-ray peak energy obtained at $\theta = 0°$ with the measurement of $E_{\gamma 0}$ obtained from study[11] of $Mg^{22}(\beta^+)Na^{22}$.

Values of $F(\tau)$ were then computed from the experimentally determined shifts ΔE_γ (corresponding to specific detection angles θ_1 and θ_2 using Eq. (3). The evaluation of the full kinematic shift $E_{\gamma 0}\beta(0)$ is discussed in Appendix A. As mentioned above, the final values for $F(\tau)$ were obtained as an average of the results obtained at several bombarding energies E_α. Since the uncertainty attached to the kinematical shift increased as E_α increased above threshold (see Appendix A), values of $F(\tau)$ obtained from spectra taken near threshold were given more weight in obtaining the final average value.

Our results are summarized in Table VII. For three transitions no Doppler shifts were discernible and upper limits on $F(\tau)$ are given. For four transitions $F(\tau)$ was close to unity. The experiments were not designed to handle such cases very well: What would be desirable for lifetimes such that $F(\tau) \simeq 1$ would be a comparison of the Doppler shifts with the Na^{22*} nuclei recoiling into different backings—including vacuum as one case.[27,29] Furthermore, for the $2.969 \rightarrow 1.952$ and $3.059 \rightarrow 1.952$ transitions the values of $F(\tau)$ given in Table VII result from two $0°-90°$ comparisons at $E_\alpha = 7.0$ MeV, while all the other Doppler shifts were observed many times.

In the absence of corroborating measurements such as mentioned above, we do not feel confident enough to infer lifetimes for the four levels for which $F(\tau)$ deviates slightly from unity. Thus, we have only set upper limits on the lifetimes of these four levels from the lower limits (two standard deviations) on $F(\tau)$

---

[31] If there were no scattering of the recoiling nuclei Eq. (5) would imply that the ion energy loss was given by $-dE/dx = K_n(v/v_0)^{-1} + K_e(v/v_0)$. This is the relation assumed previously (Refs. 21, 27, and 28) when scattering was implicitly but not explicitly taken into account.

Na[22] transition (MeV)	Stopping material	$F(\tau)$[a]	τ (psec)
$0.891 \rightarrow 0$	CaF$_2$	<0.07	>8
$1.528 \rightarrow 0$	CaF$_2$	0.089 ± 0.010	3.8 ± 0.9
$1.937 \rightarrow 0.657$	CaF$_2$	0.95 ± 0.05 (>0.85)	0.029 ± 0.03 <0.09
	Nickel	0.93 ± 0.06 (>0.81)	$0.024_{-0.024}^{+0.033}$ <0.06
$1.952 \rightarrow 0.583$	CaF$_2$	0.95 ± 0.05 (>0.85)	<0.09
$1.984 \rightarrow 0.583$	CaF$_2$	0.214 ± 0.012	1.6 ± 0.34
	Nickel	0.108 ± 0.016	1.7 ± 0.6
$2.211 \rightarrow 0.657$	CaF$_2$	<0.035	>11
$2.572 \rightarrow 0$	CaF$_2$	<0.04	>10
$2.969 \rightarrow 1.952$	CaF$_2$	0.89 ± 0.05 (>0.79)	<0.14
$3.059 \rightarrow 1.952$	CaF$_2$	0.95 ± 0.05 (>0.85)	<0.09

[a] In cases where the values measured for $F(\tau)$ are not grossly inconsistent with unity, we have indicated in parentheses the lower limits on $F(\tau)$ used in computing the corresponding upper limits on τ.

given in parentheses in the third column of Table VII. However, we note that the lifetimes inferred for the 1.937-MeV level are in good agreement with that predicted ($\tau=0.024\pm0.003$ psec) from the logft value for the β^+ decay of Mg[22] to this level.[11]

For the two remaining Na[22] transitions listed in Table VII, values of $F(\tau)$ measurably different from 0 or 1 were obtained. The γ-ray peaks corresponding to these two transitions have quite distinctive Doppler line shapes (see Figs. 2 and 3) and it was these two line shapes which we analyzed to obtain information on the nuclear stopping and scattering parameter γ_i^2. This information was then used in converting the limits on $F(\tau)$ to the mean-lifetime limits listed in Table VII. We shall now discuss these Doppler line shapes.

Doppler Line Shapes

The Doppler line shapes and line shifts of the $1.528 \rightarrow 0$ and $1.984 \rightarrow 0.583$ transitions were investigated at bombarding α energies of 4.7, 4.8, 5.0, 5.2, 5.4, 5.5, 5.6, and 7.0 MeV. The 1.528-MeV γ ray was not seen for $E_\alpha<4.6$ MeV while the 1.400-MeV γ ray was not observed for $E_\alpha<5.2$ MeV. For either case the observed line shape has two possible interpretations: (1) The shape is due to a single γ ray de-exciting a level with a lifetime such that the line shape exhibits Doppler effects, and (2) the shape results from an unresolved doublet with one member having no Doppler shift and the other having a partial Doppler shift. It was in order to decide between these two alternative explanations that the line shapes were studied at different α energies and also with both a thick CaF$_2$ target and a thin CaF$_2$ target on a nickel backing. It was found that the eight line shapes observed for the $1.528 \rightarrow 0$ transition and the five line shapes observed for the $1.984 \rightarrow 0.583$ transition with the thick CaF$_2$ target were independent

of α energy within experimental uncertainties. Since the γ-ray yield from each of these two levels changed by more than a factor of 10 over the range of E_α examined, it is extremely unlikely that either line shape is due to an unresolved doublet. Further evidence in favor of a single γ ray came from the results obtained with a 20-μg/cm^2 CaF$_2$ target evaporated onto a nickel backing. For this situation most of the γ rays are emitted from Na[22]* nuclei which are stopping in nickel. One 0° spectrum taken at $E_\alpha=5.4$ MeV was analyzed. The results for both transitions were consistent with those expected from the analysis of the results obtained with a thick CaF$_2$ target assuming a single γ ray. The Doppler line shape for the $1.984 \rightarrow 0.583$ transition with nickel backing will be presented; that for the $1.528 \rightarrow 0$ transition was not fully analyzed to determine a lifetime, since it was of poor statistical accuracy and was partially obscured by a contaminant peak of unknown origin.

The Doppler line shapes of the 1.528- and 1.400-MeV full-energy-loss peaks for the Na[22]* nuclei stopping in CaF$_2$ are shown in Figs. 12 and 13 with background subtracted. The 1.528-MeV line-shape data are from the sum of the $E_\alpha=4.7$-, 4.8-, and 5.2-MeV spectra. The 1.400-MeV line shape was obtained from the sum of the $E_\alpha=5.4$- and 5.6-MeV spectra.

The solid curves through the data points in Figs. 12 and 13 are computer fits to the line shapes using a specialization of the form of $dN(V)/dV$ given in Appendix B. A Gaussian response function was assumed for the Ge(Li) detector and this was folded into the theoretical expression for $dN(V)/dV$. The mismatch between the solid curve and the datum points at low channel numbers in Figs. 12 and 13 is just as expected, since the actual detector response has a low-energy tail[15]
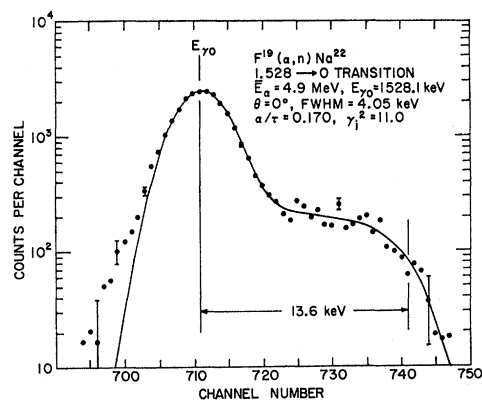

FIG. 12. The full-energy-loss peak of the 1.528-MeV γ ray corresponding to the Na[22] $1.528 \rightarrow 0$ transition observed at 0° to the beam. The γ ray results from direct feeding of the 1.528-MeV level in the F[19](α,n)Na[22] reaction initiated in a 1.0-mg/cm^2 CaF$_2$ target. The spectrum is the sum of three obtained at $E_\alpha=4.7$, 4.8, and 5.2 MeV. Background has been subtracted. The dispersion is 0.4535 keV/channel. The solid curve is a theoretical fit to the γ-ray line shape as described in the text. The parameters used in the theoretical curve are given in the figure.
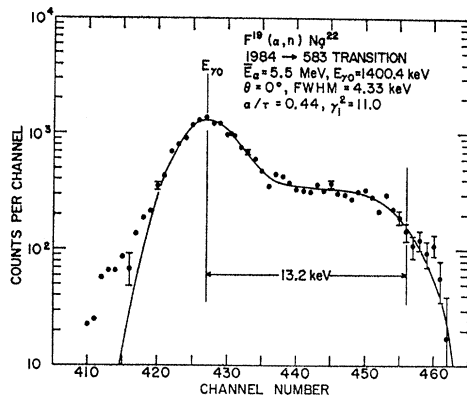
FIG. 13. The full-energy-loss peak of the 1.400-MeV γ ray corresponding to the Na^{22} 1.984 → 0.583 transition observed at 0° to the beam. The γ ray results from direct feeding of the 1.984-MeV level in the $F^{19}(\alpha,n)Na^{22}$ reaction initiated in a 1.0-mg/cm^2 CaF_2 target. The spectrum is the sum of two obtained at $E_\alpha = 5.4$ and 5.6 MeV. Background has been subtracted. The dispersion is 0.4542 keV/channel. The solid curve is a theoretical fit to the γ-ray line shape as described in the text. The parameters used in the theoretical curve are given in the figure.

which can explain the mismatch within experimental errors.[32] This tail has an area which comprises only a few percent of the total peak area; thus, neglect of the tail will cause negligible error in the values of α/τ and γ_i^2 extracted. The FWHM of the Gaussian peaks were determined from nearby γ-ray peaks which exhibited no Doppler effects. The channel corresponding to the unshifted line positions ($E_{\gamma 0}$) and the 0°–90° kinematical shift $E_{\gamma 0}\beta(0)$ of Eq. (3) were determined from the energy calibration of the spectra. The 0°–90° shifts and thus the expected excursions of $dN(V)/dV$ were 13.6 and 13.2 keV for the 1.528- and 1.400-MeV lines, respectively. The intensities of the theoretical and experimental line shapes were normalized at $E_{\gamma 0}$. The intensity of the experimental distribution at $E_{\gamma 0}$ was determined from a Gaussian fit to the energy region $E_{\gamma 0} \pm 0.5$(FWHM). The parameters just discussed were held fixed and the two remaining parameters describing the theoretical line shape, namely, α/τ and γ_i^2, were varied in discrete steps. For each set of α/τ and γ_i^2 a value of X^2, representing the goodness of fit, was calculated for the energy region from $E_{\gamma 0} + 0.5$ (FWHM) to the last datum point shown in Figs. 12 and 13. The results of this search program are illustrated in Fig. 14.

In the lower part of Fig. 14 is shown the minimum value of X^2 plotted against $K_n/K_e = [v(0)/v_0]^2/\gamma_i^2$. For each value of K_n/K_e, α/τ was varied to obtain the best fit. In the upper part of Fig. 14 are shown the resulting values of α/τ corresponding to each value of K_n/K_e.

It is quite satisfying that the two line shapes yield identical values for K_n/K_e even though α/τ is different for the two. We find for both $K_n/K_e = 0.16_{-0.06}^{+0.08}$, where the uncertainties are standard deviations. This

---

[32] This low-energy tail would completely mask any large-angle scattering effects of the type discussed in Ref. 30.

value of K_n/K_e corresponds to values of γ_i^2 of $10.7_{-4.0}^{+5.4}$ and $12.0_{-4.5}^{+5.0}$ for the 1.528- and 1.400-MeV lines, respectively. These values differ since $v(0)/v_0$ was different for the two lines and $\gamma_i^2 = (K_e/K_n)[v(0)/v_0]^2$. The value of K_n/K_e obtained in this analysis was used in obtaining the lifetime limits given in Table VII. The method used is discussed in Appendix B where the physical significance of our estimate of K_n/K_e is also discussed.

Although γ_i^2 is only roughly determined by our line-shape analysis, it is seen from the upper part of Fig. 14 that α/τ is rather insensitive to γ_i^2 so the 50% uncertainty in γ_i^2 results in a considerably smaller uncertainty in α/τ. Nevertheless, it is the largest contributor to the uncertainty in α/τ. We note that if α/τ were accurately known from some other source, then γ_i^2 (or some other parametrization of the nuclear stopping and scattering) could be determined rather accurately from Doppler line-shape analysis. This is illustrated by showing, in the lower part of Fig. 14, the
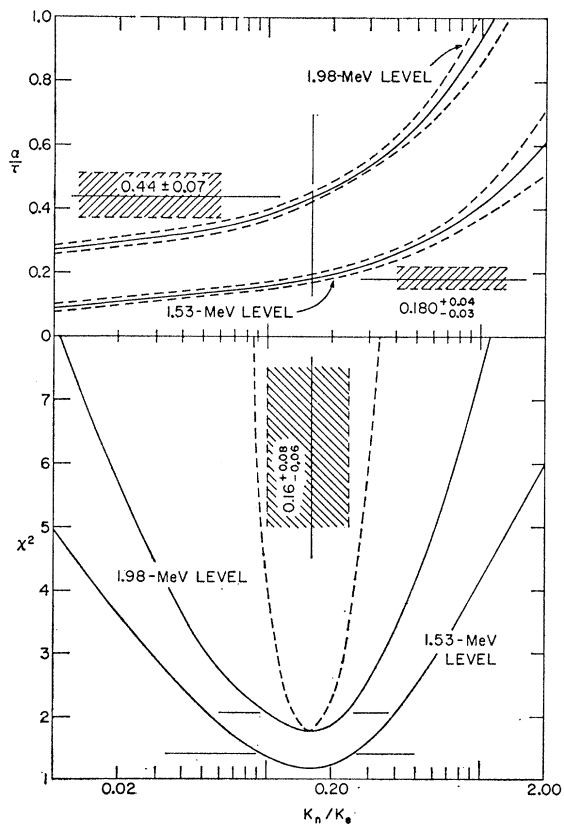

FIG. 14. Resume of the results of the two-parameter search for the best fits to the line shapes of Figs. 12 and 13. The lower part of the figure shows X^2 versus the ratio K_n/K_e for the two transitions indicated. The upper part of the figure shows the ratio α/τ as a function of K_n/K_e. The dashed curves in the upper part represent departures of one standard deviation from the solid curves for fixed values of K_n/K_e. The values of α/τ and K_n/K_e resulting from this analysis are indicated. The errors on these parameters correspond to one standard deviation. The dashed curve in the lower figure is discussed in the text.

TABLE VIII. Lower limits on radiative widths and electromagnetic transition strengths in Na²².

Transition (MeV)	Minimum Γ_γ (eV)	Minimum transition strengths (Weisskopf units)					Restrictions on J, π, and T
		$E1$	$M1$	$E2$	$M2$	$E3$	
$0.891 \to 0$	6.6×10^{-9}	1.7×10^{-8}	4.4×10^{-7}	3.9×10^{-8}	0.10	1.3×10^{8}	$1 \leqslant J(0.891) \leqslant 5$
$1.528 \to 0$	1.1×10^{-4}	5.7×10^{-5}	1.5×10^{-8}	4.4	1.1×10^{2}	5.0×10^{5}	$1 \leqslant J(1.528) \leqslant 5$, not 5^-
$1.528 \to 0.891$	2.5×10^{-6}	1.8×10^{-5}	4.6×10^{-4}	7.9	2.0×10^{2}	5.2×10^{6}	$\Delta J \leqslant 2$
$1.937 \to 0.657$	1.1×10^{-2}	1.0×10^{-2}	0.25	1.1×10^{3}	2.7×10^{4}	1.8×10^{8}	$J(1.937) = 1$, $T(1.937) = 0$
$1.952 \to 0.583$	7.3×10^{-3}	5.3×10^{-3}	0.14	5.0×10^{2}	1.3×10^{4}	7.3×10^{7}	$J(1.952) \leqslant 2$, $T(1.952) = (1)$
$1.984 \to 0.583$	2.9×10^{-4}	2.0×10^{-4}	5.0×10^{-3}	17.8	4.6×10^{2}	2.5×10^{6}	$J(1.984) \leqslant 3$, not 3^-
$2.969 \to 1.952$	4.7×10^{-3}	8.3×10^{-3}	0.22	1.5×10^{3}	3.7×10^{4}	3.8×10^{8}	$\Delta J \leqslant 1$, $\Delta T = (1)$
$3.059 \to 1.952$	7.0×10^{-3}	9.6×10^{-3}	0.25	1.4×10^{3}	3.6×10^{4}	3.1×10^{8}	$\Delta J \leqslant 1$, $\Delta T = (1)$
$3.059 \to 0.583$	7.3×10^{-5}	9.0×10^{-6}	2.3×10^{-4}	0.3	6.7	1.1×10^{4}	$J(3.059) \leqslant 3$, 3^- unlikely

χ^2-versus-K_n/K_e curve (dashed curve) which results from fixing α/τ at 0.44 for the 1.98-MeV level. From this curve we find that $K_n/K_e = 0.16 \pm 0.03$ would have resulted if α/τ were known to be 0.44.

Analysis of the Doppler line shape for the 1.984 → 0.583 transition recorded with a nickel backing was carried out in an identical fashion to that described for the CaF₂ backing. The best-fitting curve is shown in Fig. 15 together with the experimental line shape. For this line the K_n/K_e-versus-χ^2 curve had a much shallower minimum than those of Fig. 14 and K_n/K_e was only determined to $+100$ and -60%. Part of the reason for this is certainly due to the poorer statistics. Part may also be due to the fact that $\sim$10% of the γ rays arise from Na²²* nuclei decaying in the CaF₂ target and this was neglected. It is seen from Table VII that the mean lifetime obtained for the 1.984-MeV level from the nickel backing data is in excellent agreement with that obtained from the CaF₂ backing data. This gives us confidence in our analysis; but, because of the larger systematic errors involved in the former (Fig. 15) analysis, we shall adopt the lifetime resulting from the latter measurement (Fig. 13) instead of an average of the two.

C. Summary and Conclusions

Our final results for the mean lifetimes of the Na²² levels studied are listed in the last column of Table VII. We next consider the information relating to spin-parity and isotopic-spin assignments which can be inferred from these lifetimes and lifetime limits. A table of lower limits on electromagnetic transition strengths for the lower multipolarities is given in Table VIII. The matrix elements are given in Weisskopf units[33]; hereafter designated W.u. These limits follow from the lifetime limits of Table VII and the branching ratios of Table IV which were combined to give the lower limits on the partial radiative widths listed in the second column of Table VIII. For the two measured lifetimes the limits on the matrix elements correspond to an increase of the measured mean lifetime by two standard deviations. The limits also correspond to a

decrease of the branching ratio by two standard deviations in those cases in which more than one γ branch was observed. For the 0.891 → 0 transition the lower limit on Γ_γ was obtained from the limit $\tau < 10^{-7}$ sec which follows because no effects due to a lifetime of this order were observable in the various coincidence measurements of Secs. II, III, and IV, which employed a resolving time of $\sim 0.7 \times 10^{-7}$ sec.

The restrictions on spin-parity and isotopic-spin listed in the last column of Table VIII follow from sum rules,[33] systematics,[34-37] and selection rules[37,38] for electromagnetic transitions in light self-conjugate nuclei. It is clear that none of the nine transitions listed may have a multipolarity of order octupole or higher. Only the first and last may be predominantly $M2$ and for the
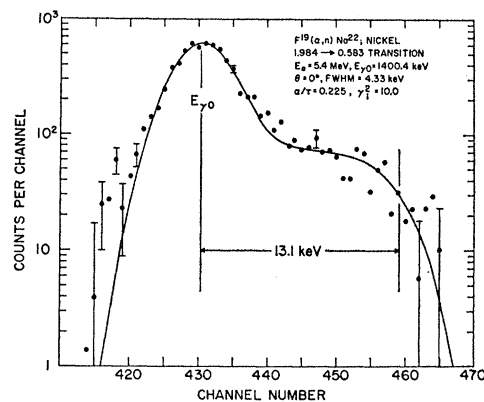

FIG. 15. The full-energy-loss peak of the 1.400-MeV γ ray corresponding to the Na²² 1.984 → 0.583 transition observed at 0° to the beam. The γ ray results from direct feeding of the 1.984-MeV level in the F¹⁹(α,n)Na²² reaction initiated in a 20-μg/cm² CaF₂ target evaporated onto a thick nickel foil. The spectrum has a dispersion of 0.4563 keV/channel and was obtained with $E_\alpha = 5.4$ MeV. Background has been subtracted. The solid curve is a theoretical fit to the γ-ray line shape as described in the text. The parameters of the theoretical fit are given in the figure.

[33] D. H. Wilkinson, in *Nuclear Spectroscopy*, edited by F. Ajzenberg-Selove (Academic Press Inc., New York, 1960), Part B, p. 862 ff.

[34] C. Van der Leun, in Proceedings of the Symposium on the Structure of Low-Medium Mass Nuclei, 1964, edited by L. W. Seagondollar (unpublished).

[35] S. J. Skorka (private communication); also (to be published).

[36] E. K. Warburton, Phys. Rev. 113, 595 (1959).

[37] E. K. Warburton, in *Isobaric Spin in Nuclear Physics*, edited by J. D. Fox and D. Robson (Academic Press Inc., New York, 1966), pp. 90–112.

[38] G. Morpurgo, Phys. Rev. 110, 721 (1958).

TABLE IX. Summary of values and restrictions on transition mixing ratios from the angular correlation and lifetime results.

Transition (MeV)	J_i	J_f	$(L+1)/L$ mixing ratio, x		Source[a]
$0.891 \rightarrow 0$	4^+	3^+	$-(2.6\pm0.5)$		Ang. corr.
$1.528 \rightarrow 0$	5^+	3^+	$\lvert x \rvert < 0.003$		τ
	3^+	3^+	$-(1.18\pm0.15)$		Ang. corr.
$1.952 \rightarrow 0.583$	$1,2$	1^+	$\lvert x(M2,E1) \rvert < 0.10$,	$\lvert x(E2,M1) \rvert < 0.56$	τ
$1.984 \rightarrow 0.583$	2^+	1^+	$x < -0.20$ or $x > 5$		Ang. corr.
	3^+	1^+	$\lvert x \rvert < 0.0014$		τ
$2.969 \rightarrow 1.952$	$\leqslant 3$	$1,2$	$\lvert x(M2,E1) \rvert < 0.06$,	$\lvert x(E2,M1) \rvert < 0.30$	τ
$3.059 \rightarrow 1.952$	$\leqslant 3$	$1,2$	$\lvert x(M2,E1) \rvert < 0.06$,	$\lvert x(E2,M1) \rvert < 0.32$	τ

[a] Ang. corr. refers to the angular-correlation results of Sec. IV, τ to the lifetime measurements of Sec. V. For the latter, the restrictions were obtained from the minimum radiative widths of Table VIII assuming quadrupole and octupole radiation cannot have a strength larger than $Z^2(=121)$ W.u.

last this is not likely. A firm upper limit to an $E2$ matrix element is Z^2 W.u.[33] and thus those transitions for which $\lvert M(E2) \rvert^2$ is greater than 121 must be predominantly dipole (i.e., $\Delta J \leqslant 1$). The four transitions with $\lvert M(M1) \rvert^2 > 0.1$ quite probably have $\Delta T = 1$.[34-38]

Some of the restrictions listed in Table VIII have been utilized in earlier parts of the paper. In the next section we shall synthesize the results of this section, summarized in Tables VII and VIII, with those of Secs. II, III, and IV, as well as with previous work.

FIG. 16. Summary of presently available information on the spin-parity and isotopic-spin assignments and branching ratios for those Na[22] levels with $E_{ex} < 3.1$ MeV, based on a synthesis of the present work with previous work (Fig. 1).

VI. SYNTHESIS OF RESULTS

A nearly complete summary of the present results together with previous work is provided by the excitation energies of Table III, the branching ratios of Table IV, and the mean lifetimes of Table VII together with the multipole-mixing restrictions summarized in Table IX. This latter table summarizes the restrictions on quadrupole/dipole or octupole/quadrupole mixing ratios provided by the present work and that of Refs. 2 and 8. The information on spin-parity and isotopic-spin assignments, excitation energies, and branching ratios is given schematically in Fig. 16.

We assume that all levels in Na[22] with $E_x < 3.1$ MeV have $T = 0$ except those indicated in Fig. 16 (the 0.657- and 1.952-MeV levels). We base this assumption on (a) the level scheme of Ne[22] (Fig. 1), (b) the Mg[24]-(d,α)Na[22] studies of Hinds et al.,[6] and (c) the lower limits on the transition strengths which are summarized in Table VIII. Argument (a) indicates that there should be only one $T = 1$ level in this energy region in addition to the $J^\pi = 0^+$, $T = 1$ 0.657-MeV level and that it should be near 1.93 MeV in excitation and have $J^\pi = 2^+$. Since the 1.528-, 1.937-, and 2.211-MeV levels do not so qualify (i.e., $J \neq 2$), the 1.952- and 1.984-MeV levels are the only possible candidates. Argument (b) is based on the fact that formation of a $T = 1$ level in the Mg[24](d,α)Na[22] is forbidden as long as there is not isotopic-spin mixing in the compound nucleus through which the reaction will at least partially proceed. Hinds et al.[6] found that all of the known Na[22] states below 3.1-MeV excitation were formed in the Mg[24](d,α)Na[22] reaction indicating isotopic-spin mixing in some stage of the reaction. However, the 0$^+$ 0.657-MeV level and the 1.952-MeV level appeared to be formed most weakly, with relative intensities in reasonable agreement with the ratio $\sim 1:5$ estimated from the spin dependence, i.e., a factor of $(2J+1)$. On the other hand, the 1.984-MeV level was quite strongly formed, the ground state being the only level more strongly formed in the energy region considered. Finally, argument (c) strongly favors a $T = 1$ assignment for the 1.952-MeV level. Three strong dipole transitions connect the 1.952-MeV level with levels which must, from argument (a) be $T = 0$; namely, the
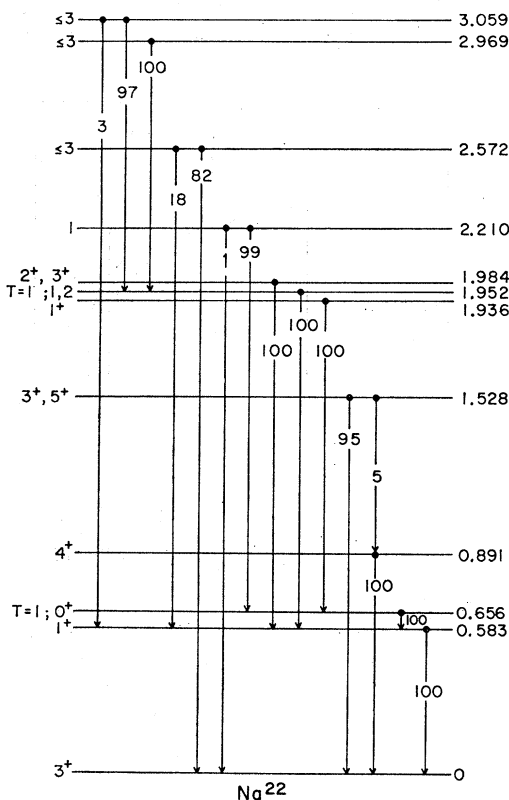
0.583-, 2.969-, and 3.059-MeV levels. We know of only two authenticated $\Delta T=0$ dipole transitions in light $(A \leqslant 40)$ self-conjugate nuclei which are stronger than the corresponding limits given in Table VIII,[33-37] and thus we would assign the 1.952-MeV level $T=1$ on the basis of argument (c) alone.

We shall now discuss the presently known information for the Na²² levels in the region $0.8 < E_x(\text{MeV}) < 3.1$ level by level. We take the first three levels of Na²² as well understood, but note that the lifetime of the 0.657-MeV level remains to be measured.[7]

The 0.891-MeV level. Consideration of the lifetime limit for this level (Table VIII) and the appearance of a $P_4(\cos\theta)$ term in its angular distribution (Table V) and correlation (Table VI) limit the spin to $2 \leqslant J \leqslant 5$. The spin is fixed as $J=4$ from the angular correlation results (Fig. 8 and Ref. 8). The parity is assigned as even by the Na²³(d,t)Na²² results of Vogelsang and McGruer.[39] The lifetime remains to be measured.

The 1.528-MeV level. The spin is limited to $2 \leqslant J \leqslant 5$ from the lifetime limit (Table VIII), angular distribution measurement (Table V), and the angular correlation measurement (Table VI) for the same reasons as for the 0.891-MeV level. The angular correlation results (Fig. 9 and Ref. 2) eliminate $J=2$ and 4. The lifetime limit eliminates $J^\pi=5^-$ and, together with the mixing ratio of the 1.528 → 0 transition demanded for $J=3$ (Table IX), eliminates $J^\pi=3^-$; thus $J^\pi=3^+$ or 5^+. Both of these are allowed by all the γ-ray studies.

Plane-wave analysis of the Na²³(d,t)Na²² reaction leading to this level appears to yield $J^\pi \leqslant 4^+$ which would select the $J^\pi=3^+$ alternative.[39] On the other hand, results from the Ne²⁰(α,d)Na²² reaction are stated[40] to give a strong preference for a $J^\pi=5^+$ assignment to the 1.528-MeV level. That these two direct-reaction results give conflicting spin assignments is not surprising, since each is based on a model-dependent analysis which does not approach the rigor possible in the analysis of studies of electromagnetic radiation. We note that if the 1.528-MeV level turns out to be 5^+, as is favored by theory,[3-5] then some doubt must be attached to the even-parity assignment to the 0.891-MeV level from the Na²³(d,t)Na²² reaction.

The $M1$ and $E2$ strengths of the 1.528 → 0 transition (Table X) appear quite reasonable for either $J^\pi=3^+$ or 5^+. We have no information on the quadrupole/dipole mixing ratio, $x(E2/M1)$, for the 1.528 → 0.891 transition. From the measured branching and lifetime we have only the restrictions on possible $M1$ and $E2$ strengths, in W.u. of $|M(M1)|^2 \leqslant 4.2 \times 10^{-3}$ and $|M(E2)|^2 \leqslant 72$. From the particular equality which must hold if the transition is either pure dipole or pure quadrupole, we conclude that the transition probably has significant components of both $M1$ and $E2$ radiation.

[39] W. F. Vogelsang and J. N. McGruer, Phys. Rev. 109, 1663 (1958).
[40] E. Rivet, G. H. Pehl, J. Cerny, and B. G. Harvey, Phys. Rev. 141, 1021 (1966).

TABLE X. Electromagnetic transition strengths for some transitions in Na²².

Transition (MeV)	J_iT_i	J_fT_f	Multipole	$|M|^2$ (Weisskopf units)
0.583 → 0	1⁺,0	3⁺,0	E2	0.0092±0.0008
1.528 → 0	5⁺,0	3⁺,0	E2	$6.6_{-1.3}^{+2.1}$
1.528 → 0	3⁺,0	3⁺,0	{M1	$(1.0\pm0.3)\times10^{-3}$
			{E2	3.8±1.3
1.984 → 0.583	3⁺,0	1⁺,0	E2	$25.3_{-4.4}^{+6.8}$

The 1.937-MeV level. This level has been shown to have $J=1$ by consideration of three independent phenomena: the positron decay of Mg²², the 1.937 → 0.657 angular correlation results (Fig. 10), and the lifetime limit (Table VIII). The first of these fixes the parity as even.[11]

The 1.952-MeV level. As already discussed we assign this level $T=1$ and find no previous work in disagreement with this assignment. From a comparison with Ne²² (Fig. 1) it is therefore $J^\pi=2^+$ although experimentally we have only shown $J=1$, 2 (from the lifetime limit of Table VIII and the angular-distribution results of Table V). The absence of a ground-state transition from this level (Table IV) is quite striking and indicates a strong nuclear-structure effect.

The 1.984-MeV level. The angular distribution and correlation results both indicate $J \geqslant 2$ since a $P_4(\cos\theta)$ term is observed. The lifetime limit immediately rules out $J>3$ and also $J^\pi=3^-$ (Table VIII). For $J=2$ we have $x(M2/E1) < -0.2$ (Table IX) for the 1.984 → 0.583 transition: this means $|M(M2)|^2 > 18.4$ W.u. Such a large $\Delta T=0$ $M2$ rate is certainly not reasonable, and so $J^\pi=2^+$ or 3^+. There is no strong preference for either assignment but we note that 3^+ is slightly disfavored because the $E2$ strength of the 1.984 → 0.583 transition would be $25_{-4.4}^{+6.8}$ W.u. for $J^\pi=3^+$ (Table X) which is indeed quite strong.

As in the case of the 1.952-MeV level, the weakness of the ground-state transition (Table IV) indicates a strong nuclear structure effect.

The 2.211- and 2.572-MeV levels. Our results for these two levels are in good agreement with previous work,[2] and add little new information regarding spin-parity, isotopic-spin, and γ-ray branching ratios. There is no experimental preference for the parity of either state. A startling result is the very long lifetimes of both levels (Table VII). Each level has several different possible modes of decay by dipole and quadrupole radiation, including a $\Delta T=1$ dipole transition to the $T=1$ 1.952-MeV level (assuming the 2.572-MeV level has $J=1$, 2, or 3). Thus the weak transition strengths of these three possible decay modes is indeed a striking effect.

The 2.969- and 3.059-MeV levels. We find both levels decay by dipole transitions to the 1.952-MeV level and so both have $J \leqslant 3$ ($J=1$, 2, or 3 if the 1.952-MeV level has $J^\pi=2^+$). The 3.059-MeV level also has a weak γ-ray branch to the 0.583-MeV level. These decay modes

are consistent with expectations for levels with $T=0$ and $J=2$, or 3, either parity.

We have made relatively few references to earlier γ-ray studies of Na^{22} mainly because most of these are adequately summarized by Endt and Van der Leun[7] and because, aside from some tentative speculations, we have found no points of disagreement with earlier work. Mention should perhaps be made of the Ne^{21}-(p,γ)Na^{22} work of Arnell and Wernbom-Selin[41] who suggested a decay scheme for the 1.9-MeV triplet which is in agreement with our findings, but who incorrectly inferred that the major decay mode of the 3.059-MeV level is to the ground state.

APPENDIX A. KINEMATICS OF THE F$^{19}(\alpha,n)$Na^{22} REACTION NEAR THRESHOLD

At the threshold for production of an endothermic (α,n) reaction the reaction products, having zero energy in the center-of-mass system, are all emitted with the same velocity along the beam axis (z axis). For beam energies close to threshold $[E_\alpha \lesssim 2E_\alpha(\mathrm{th})$, where $E_\alpha(\mathrm{th})$ is the threshold energy] the speed of the outgoing heavy particle is fairly well defined and its direction is confined, relative to the beam axis, to a rather narrow cone of half-angle $\phi_{\max}$. We wish in this Appendix to examine the extent of the variation in the heavy-particle velocity (magnitude and direction) and the effect of this variation on the Doppler-shift measurements reported in Sec. V.

For a reaction of the type $M_2(m_1,m_4)M_3^*$, the center-of-mass velocity (in units of the speed of light) is

$$\beta_{\mathrm{c.m.}} = (2m_1E_1)^{1/2}/(m_1+M_2), \qquad \text{(A1)}$$

where all masses and energies are in MeV and E_1 is the beam energy in the laboratory system. The corresponding z component of velocity for the excited nucleus M_3^* at the moment of emission ($t=0$) is

$$\beta_z(0) = \beta_{\mathrm{c.m.}}[1+\gamma^{-1}\cos\theta_{\mathrm{c.m.}}], \qquad \text{(A2)}$$

where $\theta_{\mathrm{c.m.}}$ is the center-of-mass angle of the outgoing nucleus M_3^*, γ^{-1} is the ratio of the speed of M_3^* in the center-of-mass system to the speed of the center of mass in the laboratory system and is given by

$$\gamma^{-1} = \left\{ \frac{M_2m_4}{m_1M_3^*}\left[1+\frac{m_1+M_2}{M_2}Q/E_1\right]\right\}^{1/2}, \qquad \text{(A3)}$$

where the Q value is given by (Q_0-E_x) with Q_0 and E_x being the Q value for the ground-state reaction and the excitation energy of the level of M_3 in question. The magnitude of the component of velocity perpendicular to the z axis $\beta_\perp(0)$ is

$$\beta_\perp(0) = \beta_{\mathrm{c.m.}}\cdot\gamma^{-1}\sin\theta_{\mathrm{c.m.}}. \qquad \text{(A4)}$$

Because of the axial symmetry involved, this component of velocity does not contribute to the *average* shift in

[41] S. E. Arnell and E. Wernbom-Selin, Arkiv Fysik **27**, 1 (1964).

energy of the γ rays emitted in a given direction from an ensemble of nuclei; it also does not contribute to the Doppler line shape of those γ rays observed at 0° to the beam. (In general, however, it will contribute to the line shape and, in particular, it contributes all of the Doppler *broadening* for observation of γ rays at 90° to the beam.) Because $\beta_\perp(0)$ does not contribute to the average Doppler shift or to the 0° line shape, $\beta_z(0)$ is the quantity of interest and we wish to examine the uncertainties introduced by neglecting the spread in the value of $\beta_z(0)$ implied by Eq. (A2) as was done in Sec. V of the text.

For the F$^{19}(\alpha,n)$Na^{22} reaction Eqs. (A2) and (A3) become

$$\beta_z(0) = 0.40305\times10^{-2}E_\alpha^{1/2}(1+\gamma^{-1}\cos\theta_{\mathrm{c.m.}}) \qquad \text{(A5)}$$

and

$$\gamma^{-1} = 0.4666[1+1.2107(Q/E_\alpha)]^{1/2}, \qquad \text{(A6)}$$

where E_α is the laboratory energy of the α-particle beam.

From Eq. (A2) or (A5) we see that γ^{-1} is the maximum possible fractional variation in $\beta_z(0)$. The maximum angular deviation of $\beta(0)$ from the z axis, $\phi_{\max}$, is given by $\sin^{-1}\gamma^{-1}$, so that $\cos\phi_{\max}=(1-\gamma^{-2})^{1/2}$. The parameters $\gamma^{-1}(=|\Delta\beta_{\max}/\beta_{\mathrm{c.m.}}|)$ and $(1-\gamma^{-2})^{1/2}$ are shown in Fig. 17 as a function of the ratio of the beam energy increment above threshold to the threshold energy $E_\alpha(\mathrm{th})$.[42] The threshold energy is [see Eq. (A3)] equal to $-[(m_1+M_2)/M_2]Q$ MeV which for the F$^{19}(\alpha,n)$Na^{22} reaction is $-1.2107Q$ MeV.

The Doppler-shift measurements described in Sec. V were carried out at values of $[E_\alpha-E_\alpha(\mathrm{th})]/E_\alpha(\mathrm{th})$ between 0.07 and 0.25. This region is indicated in Fig. 17. For instance, the lifetime limit for the Na^{22} 2.211-MeV level was obtained from data taken at $E_\alpha=5.4$ MeV for which energy $[E_\alpha-E_\alpha(\mathrm{th})]/E_\alpha(\mathrm{th})=0.071$, while this ratio was 0.155 for the study of the 1.984-MeV level at an average α energy of 5.5 MeV.

For an isotropic distribution of the outgoing neutrons in the center-of-mass system the mean value of $\beta_z(0)$, $\langle\beta_z(0)\rangle$, for an ensemble of recoiling Na^{22*} ions is just $\beta_{\mathrm{c.m.}}$ since $\langle\beta_z(0)\rangle$ is given by

$$\langle\beta_z(0)\rangle = \beta_{\mathrm{c.m.}}[1+\gamma^{-1}\langle\cos\theta_{\mathrm{c.m.}}\rangle], \qquad \text{(A7)}$$

where $\langle\cos\theta_{\mathrm{c.m.}}\rangle$ indicates an average over the differential cross section of the reaction. From consideration of many experimental angular distributions we have found that 0 ± 0.33 is a good *a priori* estimate for $\langle\cos\theta_{\mathrm{c.m.}}\rangle$. The uncertainty is quite conservative in that we are not aware of any experimental angular distributions which give values of $\langle\cos\theta_{\mathrm{c.m.}}\rangle$ further than 0.66 from 0 and most fall within 0.33 of 0. (One reason for this is that $\cos\theta_{\mathrm{c.m.}}$ is weighted by $\sin\theta_{\mathrm{c.m.}}$ in obtain-

[42] The maximum possible angular deviation of $\beta(0)$ from the z axis illustrated in the upper part of Fig. 17 is not pertinent to the analysis of Doppler effects since we are only interested in $\beta_z(0)$. This figure is shown, however, because it is pertinent to target design (thickness, angle of target normal to beam, etc.).

ing $\langle\cos\theta_{c.m.}\rangle$.) Using 0 ± 0.33 for $\langle\cos\theta_{c.m.}\rangle$ results in $0.33\gamma^{-1}$ as the fractional uncertainty in $\langle\beta_z(0)\rangle$; i.e.,

$$\langle\beta_z(0)\rangle{\simeq}\beta_{c.m.}.[1\pm0.33\gamma^{-1}]. \qquad (A8)$$

Equation (A8) was used in evaluating the limits or values of $F(\tau)$, the Doppler-shift attenuation coefficient, given in Table VII.

We now consider the effects of the spread of initial velocities $\beta_z(0)$, as given by Eq. (A5) on the Doppler line shapes. First there is the spread in $\beta_z(0)$ due to the fact that E_α varies from the beam energy to the effective threshold energy. For both of the line shapes studied this effect introduces an uncertainty in $\beta_z(0)$, and thus in the maximum γ-ray energy, of $\sim1\%$ and this is negligible. More important is the spread in $\beta_z(0)$ resulting from the angular distribution of the reaction products, which corresponds in Eq. (A5) to a variation of $\cos\theta_{c.m.}$ from $+1$ to -1. The resultant spread in $\beta_z(0)$ introduces a corresponding spread in the kinematical Doppler shift with a maximum excursion about $E_{\gamma0}\beta_{c.m.}$ of $\pm E_{\gamma0}\beta_{c.m.}.\gamma^{-1}$. Experimentally we found that the Doppler broadening of fast transitions at $0°$ to the beam is simulated for present purposes by a Gaussian distribution with a FWHM of $\sim E_{\gamma0}\beta_{c.m.}.\gamma^{-1}$. This is in agreement with estimates assuming an isotropic angular distribution. For the two Doppler line shapes studied (Sec. V) the spread $E_{\gamma0}\beta_{c.m.}.\gamma^{-1}$ is ~2 keV. When this is folded into the detector resolution function having a FWHM of ~4 keV it is found to result in a $\sim10\%$ increase in the effective FWHM near the high-energy end of the line-shape distribution decreasing to a negligible effect near the low-energy end. This broadening was examined by increasing the assumed FWHM of the detector and examining the resultant change in the high-energy end of the line shape. The effect was thus found to have negligible influence on our analysis. We note that for the line shapes observed at higher α energies (7.0 MeV) this effect is expected to be larger and, in fact, was observed as an excess of counts at the very high-energy end of the Doppler line shape.

APPENDIX B. PHENOMENOLOGICAL APPROACH TO THE DOPPLER-SHIFT ATTENUATION METHOD (DSAM)

1. General

As discussed in Sec. V, the quantities of interest to us for analysis of DSAM experiments are $F(\tau)$ and $dN(V)/dV$. These as well as the projected range R_z of heavy ions in matter will be considered in this Appendix. We calculate these three quantities from a phenomenological representation of $M_1(dv_z/dt)$,

$$-M_1(dv_z/dt)=K_n(v_z/v_0)^{-1}+K_e(v_z/v_0), \qquad (B1)$$

where M_1 is the mass of the moving ion and $v_0=c/137$. It is our intention to present a justification of this

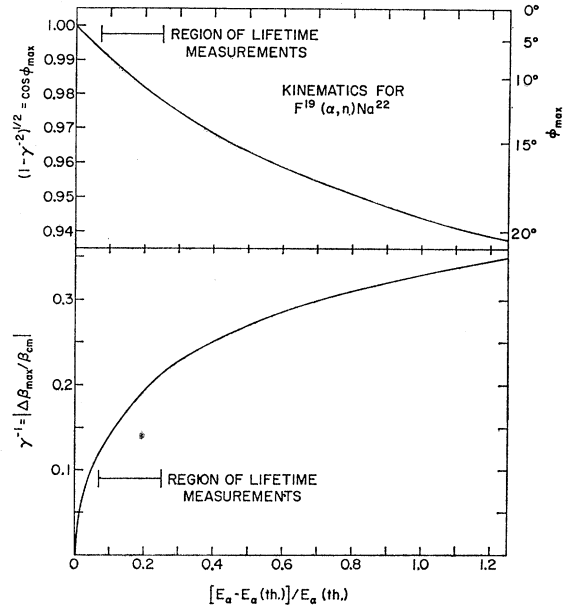FIG. 17. Kinematical parameters of interest for application of the Doppler-shift attenuation method to the $F^{19}(\alpha,n\gamma)Na^{22}$ reaction (see text).

representation and then to use it to derive expressions for $F(\tau)$, $dN(V)/dV$, and R_z.

A general identity for $M_1(dv_z/dt)$ is

$$M_1(dv_z/dt)=(dv_z/dv)dE/dx, \qquad (B2)$$

where x is measured along the path of the ion. The energy loss of heavy ions in matter dE/dx is composed of an electronic part $(dE/dx)_e$ in which the ion loses energy to electrons, and a nuclear part $(dE/dx)_n$ in which the ion loses energy by interaction with atoms as a whole. The former is essentially a continuous process with small energy losses per event and very little deflection of the moving ions. In contrast, nuclear, or quasi-elastic collisions, result in large energy losses per event and large deflections of the moving ion.[43]

For an individual ion both (dv_z/dt) and $(dE/dx)_n$ are discontinuous functions due to nuclear scattering. However, we consider an ensemble of moving ions which because of the discrete nature of the energy loss process will have a distribution of velocities and we take v and v_z to represent the mean value of these distributions with $E=\frac{1}{2}M_1v^2$. In this case (dv_z/dt) and $(dE/dx)_n$ are continuous functions as well. In the next section we shall consider $(dE/dx)_e$; $(dE/dx)_n$ and dv_z/dv are considered in Sec. 3 of this Appendix.

2. Electronic Stopping

Lindhard and Scharff[43,44] have found, on the basis of Thomas-Fermi arguments, that for velocities below

[43] J. Lindhard, M. Scharff, and H. E. Schiøtt, Kgl. Danske Videnskab. Selskab, Mat.-Fys. Medd. 33, No. 14 (1963).
[44] J. Lindhard and M. Scharff, Phys. Rev. 124, 128 (1961).

$\sim Z_1^{2/3}v_0$ the electronic stopping power is given by

$$-(dE/dx)_e = \frac{\xi_e 8\pi N e^2 a_0 Z_1 Z_2 v}{v_0 (Z_1^{2/3}+Z_2^{2/3})^{3/2}}, \qquad (B3)$$

where N is the number of stopping atoms per cc; $v_0\ (\equiv c/137)$ is the velocity of an electron in the first Bohr orbit of hydrogen while a_0 is the radius of this orbit, e is the electron charge, Z_1 and Z_2 are the atomic numbers of the projectile and target atoms, respectively, and v is the velocity of the projectile. The constant ξ_e should lie roughly between 1 and 2 and may vary as $Z_1^{1/6}$. It has become customary to set ξ_e equal to $Z_1^{1/6}$ and refer to the resulting expression for $-(dE/dx)_e$ as the Lindhard-Scharff estimate. Equation (B3) has the form

$$-(dE/dx)_e = K_e(v/v_0). \qquad (B4)$$

For $\xi_e = Z_1^{1/6}$, K_e is given by

$$K_e\left(\frac{\text{keV cm}^2}{\mu g}\right) = 11.53\left(\frac{Z_2}{A_2}\right)\frac{Z_1^{7/6}}{(Z_1^{2/3}+Z_2^{2/3})^{3/2}}, \qquad (B5)$$

where A_2 is the atomic weight (C^{12} scale) of the stopping material. In the present experiments (Sec. V) $v(0)$ $\simeq 1.3v_0$ which satisfies the approximate restriction on the range of validity of Eq. (B4), $v \lesssim Z_1^{2/3}v_0$.

Essentially all of the systematic experimental stopping data for $v \lesssim Z_1^{2/3}v_0$ has come from the work of Duckworth and his collaborators[45] and from the Manchester group.[46-48] The former measurements include a systematic investigation of the stopping in boron, carbon, and aluminum of ions with Z_1 between 3 and 11 and v/v_0 between 0.1 and 0.6. The Manchester measurements are in fairly good agreement among themselves and include data for $Z_1 = 2$, 6, 7, 8, and 10 and stopping materials of carbon, aluminum, nickel, silver, and gold with v/v_0 between 0.9 and 3.5. For stopping in carbon and aluminum, these two sets of data overlap in Z_1 but not in v/v_0. In these cases the data are generally in quite good agreement in the sense that a smooth curve generally joins the two sets of data in a $(dE/dx)_e$-versus-v/v_0 plot for a particular Z_1, Z_2 combination. In the region $v/v_0 \lesssim 1.5$ of interest here, both sets of data show some deviation from the proportionality of $(dE/dx)_e$ to v/v_0 predicted by Eq. (B4). Nevertheless, the Lindhard-Scharff estimate gives a representation of the velocity dependence of $-(dE/dx)_e$ which is good enough for present purposes.

For all Z_1, Z_2 combinations the magnitude of the electronic stopping power found by these two groups lies in the range predicted by Eq. (B3), i.e., $1 \lesssim \xi \lesssim 2$. An interesting phenomenon is that for a particular stopping material the values of K_e extracted from the data show a periodic variation with Z_1 about the Lindhard-Scharff estimate.[45] For $2 \lesssim Z_1 \lesssim 10$, K_e is larger than predicted by Eq. (B5) while for $10 \lesssim Z_1 \lesssim 15$, K_e is smaller than this prediction.

For the stopping of Na ions in boron, carbon, and aluminum Duckworth and his collaborators[45] find that K_e is smaller than the Lindhard-Scharff estimate, Eq. (B5), by factors of 0.76 ± 0.07, 0.80 ± 0.06, and 0.85 ± 0.06, respectively. Since this ratio appears to be relatively insensitive to stopping material we assume that the values of K_e for Na^{22} ions stopping in CaF_2 and nickel are 0.85 times the Lindhard-Scharff estimate and shall assign a 15% error to these values. We adopt 0.85, which is appropriate for stopping in aluminum, rather than the average of the three ratios since the average Z_1 for CaF_2 is closer to that of aluminum than to that of boron and carbon. The uncertainty in K_e is assumed to include the uncertainty due to deviations from the functional form of Eq. (B4), the uncertainty in the extrapolation to different stopping materials, and the uncertainty in the original stopping power measurements. This procedure gives values of K_e of 2.27 ± 0.34 keV cm^2/μg and 1.44 ± 0.22 keV cm^2/μg for Na^{22} ions stopping in CaF_2 and nickel, respectively. The electronic stopping times, $\alpha(=M_1v_0/K_e\rho)$, corresponding to these two values of K_e are 0.69 ± 0.10 psec and 0.39 ± 0.06 psec, respectively.[49]

3. Nuclear Stopping and Scattering

Theoretical estimates of $(dE/dx)_n$ are illustrated in Fig. 18 where we have considered Na^{24} ions stopping in aluminum to exemplify our approach.

The first estimate of this quantity was given by Bohr in his pioneer work on the energy loss and range of heavy ions.[50] It is given by

$$-(dE/dx)_n = \frac{4\pi N Z_1^2 Z_2^2 e^4}{M_2 v^2}\ln\frac{a M_1 M_2 v^2}{(M_1+M_2)Z_1 Z_2 e^2}, \qquad (B6)$$

where M_1 and M_2 refer to the moving ion and stopping material, respectively, and the screening parameter a is given by,[43]

$$a = 0.885 a_0 (Z_1^{2/3}+Z_2^{2/3})^{-1/2}.$$

Another estimate, convenient for some purposes, im-

[45] A. Van Wijngaarden and H. E. Duckworth, Can. J. Phys. **40**, 1749 (1962); J. H. Ormrod and H. E. Duckworth, *ibid.* **41**, 142 (1963); J. H. Ormrod, J. R. MacDonald, and H. E. Duckworth, *ibid.* **43**, 225 (1964); J. R. MacDonald, J. H. Ormrod, and H. E. Duckworth, Z. Naturforsch. **21**, 130 (1966).

[46] D. I. Porat and K. Ramavataram, Proc. Roy. Soc. (London) **A252**, 394 (1959); **77**, 97 (1961); **78**, 1135 (1961).

[47] W. R. Phillips and F. H. Read, Proc. Phys. Soc. (London) **81**, 1 (1963); P. H. Barker and W. R. Phillips, Proc. Phys. Soc. (London) **86**, 379 (1965).

[48] W. Booth and I. S. Grant, Nucl. Phys. **63**, 481 (1965).

[49] We have explicitly given K_e, which has the dimensions of dE/dx, the units keV cm^2/μg in Eq. (B5). Thus α has the units of time when we define it as $M_1v_0/K_e\rho$, where ρ is the density of the target. Thus the uncertainty in the density of the stopping material is included in that of α. We shall sometimes use M_1v_0/K_e for α since this is more appropriate when considering ion ranges in units of μg/cm^2.

[50] N. Bohr, Kgl. Danske Videnskab. Selskab, Mat.-Fys. Medd. **18**, No. 8 (1948).
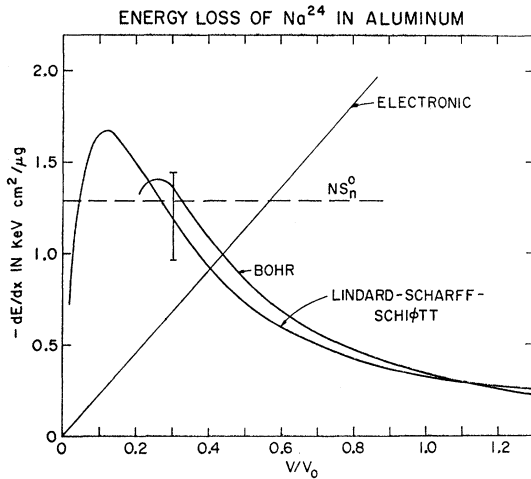
ENERGY LOSS OF Na²⁴ IN ALUMINUM

FIG. 18. The energy loss of Na²⁴ ions in aluminum. The electronic energy loss $K_e(v/v_0)$ is shown with K_e equal to 2.29 keV cm²/μg as given by the measurements reported in Ref. 45. The other three curves are estimates of the nuclear energy loss due to collisions of Na²⁴ and Al²⁷ atoms. The estimate labeled Bohr is from Ref. 50. It is not expected to be as accurate as the estimate of Lindhard, Scharff, and Schiøtt (Ref. 43) for $v/v_0 \lesssim 0.8$. For $v/v_0 \gtrsim 0.8$ these two estimates are practically indistinguishable. A rough estimate of the uncertainty of the Lindhard-Scharff-Schiøtt prediction is ∼20% for $v/v_0 > 0.25$, as indicated by the error bar. This prediction is quite uncertain for $v/v_0 \lesssim 0.25$. The constant nuclear stopping estimate NS_n^0 of Ref. 43 is sometimes used for $v/v_0 \lesssim 0.3$.

plies a constant nuclear stopping cross section S_n^0. It is quoted by Lindhard, Scharff, and Schiøtt[43] and is given by[51]

$$- (dE/dx)_n = NS_n^0 = (\pi^2/2.407)$$
$$\times Ne^2 a Z_1 Z_2 M_1 (M_1 + M_2)^{-1}. \quad (B7)$$

A more refined estimate than either of the above is given by Lindhard et al.[43] It is expressed in terms of a numerical integral and is given graphically in Fig. 18 together with the estimates implied by Eqs. (B6) and (B7) for Na²⁴ ions stopping in Al.

We define $\langle \cos\phi(t) \rangle$, where $\phi(t)$ was introduced in Sec. V, by the equation

$$v_z(t) = v(t) \langle \cos\phi(t) \rangle. \quad (B8)$$

The quantity $\langle \cos\phi(t) \rangle$ was estimated with initial velocities $v(0)/v_0$ equal to 1.3 for Na²⁴ ions stopping in aluminum from approximations given by Blaugrund.[52] This gives $\langle \cos\phi(t) \rangle$ as a function of v/v_0 from which dv_z/dv can be calculated using Eq. (B8). From this,

[51] Lindhard et al. (Ref. 43) introduce dimensionless measures of distance and energy

$$\rho = RNM_2 \times 4\pi a^2 \frac{M_1}{(M_1+M_2)^2} \text{and} \quad \epsilon = \frac{aM_2}{Z_1 Z_2 e^2 (M_1+M_2)} E,$$

where R is the range measured along the path of the moving ion. In terms of these the stopping cross section $d\epsilon/d\rho$ due to Bohr, Eq. (B6), is $\ln(2\epsilon)/2\epsilon$ and NS_n^0 is 0.3264. In these units these two estimates, as well as the Lindhard-Scharff-Schiøtt estimate, are universal, i.e., are independent of the (Z_1, M_1), (Z_2, M_2) combination.

[52] A. E. Blaugrund, Nucl. Phys. 88, 501 (1966).

$M_1 dv_z(t)/dt$ was calculated as a function of v_z/v_0 by using Eq. (B2) and taking dE/dx to be the sum of $K_e(v/v_0)$ plus the Lindhard-Scharff-Schiøtt estimate for $(dE/dx)_n$. The resulting expression for $M_1(dv_z/dt)$, which is a function of v_z/v_0, we separate into two terms as follows:

$$-M_1(dv_z/dt) = (dv_z/dv)(dE/dx)$$
$$= -M_1(dv_z/dt)_n + K_e(v_z/v_0). \quad (B9)$$

Equation (B9) defines the quantity $-M_1(dv_z/dt)_n$. In the absence of scattering, $K_e(v_z/v_0) = K_e(v/v_0) = -(dE/dx)_e$ and $M_1(dv_z/dt)_n = (dE/dx)_n$, but because of scattering these relations are not true. Thus, with K_e obtained by the procedures described in Sec. 2 of this Appendix, $-M_1(dv_z/dt)_n$, as defined by Eq. (B9), includes the difference between $K_e(v/v_0)$ and $K_e(v_z/v_0)$ as well as the more direct effects of nuclear stopping and scattering. The solid curve of Fig. 19 illustrates $-M_1(dv_z/dt)_n$ corresponding to Eq. (B9) for our example of Na²⁴ ions stopping in Al with $v(0)/v_0 = 1.3$. Also shown in Fig. 19 is the curve of $-M_1(dv_z/dt)_n$ which would pertain if there were no nuclear scattering, i.e., $\cos\phi(t) = 1.0$.

We now wish to introduce a phenomenological representation for $-M_1(dv_z/dt)_n$ which expresses it as a simple analytical function of v_z/v_0. We use $K_n(v_z/v_0)^{-1}$ so that $-M_1(dv_z/dt)$ is represented by Eq. (B1). The $K_n(v_z/v_0)^{-1}$ representation of $-M_1(dv_z/dt)_n$ is illustrated
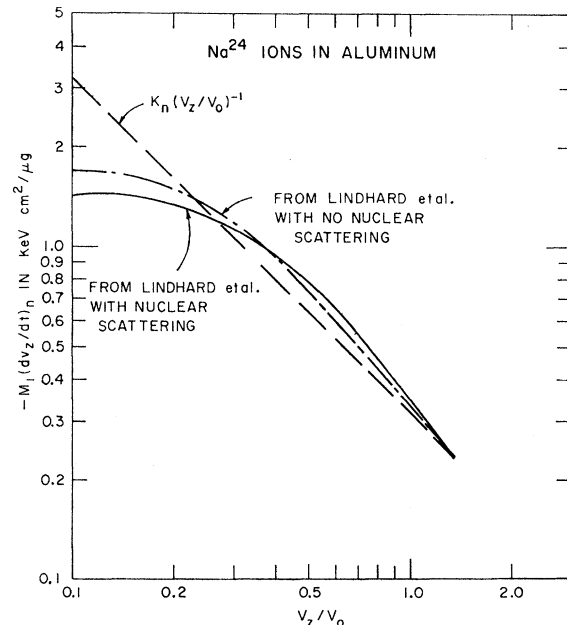

FIG. 19. Curves of $-M_1 dv_z/dt$ versus v_z/v_0. The dot-dashed curve is the same as the Lindhard-Scharff-Schiøtt curve of $(dE/dx)_n$ versus v/v_0 shown in Fig. 18 since for no scattering $v_z(t) = v(t)$ and $M_1 dv_z/dt = dE/dx$. The solid curve includes the effects of scattering for $v(0)/v_0 = 1.3$ (as explained in the text) such that $-M_1(dv_z/dt)$ is given as the sum of this curve plus $K_e(v_z/v_0)$. The dashed curve labeled $K_n(v_z/v_0)^{-1}$ is our phenomenological representation of the solid curve.

by the dashed curve of Fig. 19. K_n was fixed by setting it equal to Bohr's estimate of $(dE/dx)_n$ at $v=v_0$.

We emphasize that $-M_1(dv_z/dt)_n$ is a function of $v(0)/v_0$ and that the solid curve of Fig. 19 is for $v(0)/v_0=1.3$. For $v(0)/v_0>1.3$ the correction for nuclear scattering is small for the velocity region $v_z/v_0\gtrsim1.0$ and is quite similar to that for $v(0)/v_0=1.3$ in the region $v_z/v_0<1.0$. Thus the solid curve of Fig. 19 is a good estimate of $-M_1(dv_z/dt)_n$ for $v(0)/v_0\gtrsim1.0$. As $v(0)/v_0$ decreases below 1.0 the nuclear scattering correction becomes more and more important and is such as to bring the $M_1(dv_z/dt)_n$ curve, extracted from the Lindhard-Scharff-Schiøtt estimate of $(dE/dx)_n$, into closer agreement with the $K_n(v_z/v_0)^{-1}$ approximation. The net effect of this is that $K_n(v_z/v_0)^{-1}$ is a fairly good approximation to $-M_1(dv_z/dt)_n$ for $v_z\gtrsim0.25v(0)$ with $v(0)/v_0\gtrsim0.1$. In present day DSAM experiments $v_z<0.25v(0)$ is a region of little importance since uncertainties in $-M_1(dv_z/dt)_n$ in this region contribute little uncertainty to $F(\tau)$ and this region is obscured by the stopped component in $dN(V)/dV$.

4. Representation of Projected Ranges

We define the range parameter R_z by the expression,

$$R_z=\int_0^{v(0)}\frac{dv_z}{-dv_z/dz}=\int_0^{v(0)}\frac{M_1v_zdv_z}{-M_1(dv_z/dt)}. \quad \text{(B10)}$$

We shall associate R_z with the most probable projected range of a monoenergetic ensemble of ions stopping in matter with v_z representing the mean z component of velocity of these ions. In general, the range distribution is not symmetric so that the mean range is somewhat different from the most probable range. Physical considerations lead us to believe that R_z, as defined in Eq. (B10), is more closely associated with the most probable projected range than with the mean projected range and that the uncertainty in this association is of the order of the difference between the two.

We wish to derive an expression for R_z from our phenomenological representation of $M_1(dv_z/dt)$. We first generalize this latter expression to

$$-M_1(dv_z/dt)=K_n^{(m)}(v_z/v_0)^{-m}+K_e(v_z/v_0). \quad \text{(B11)}$$

Then, using Eq. (B10), we obtain

$$R_z=\alpha v(0)[1-F(\gamma_i^{(m)})], \quad \text{(B12a)}$$

where

$$F(\gamma_i^{(m)})=\frac{1}{\gamma_i^{(m)}}\int_0^{\gamma_i^{(m)}}\frac{dz}{z^{m+1}+1} \quad \text{(B12b)}$$

and

$$\gamma_i^{(m)}=(K_e/K_n^{(m)})^{1/(m+1)}v(0)/v_0, \quad \text{(B12c)}$$

with $\alpha=M_1v_0/K_e$. For $m=0$ and 1 the integral in Eq. (B12b) can be solved to give analytical expressions

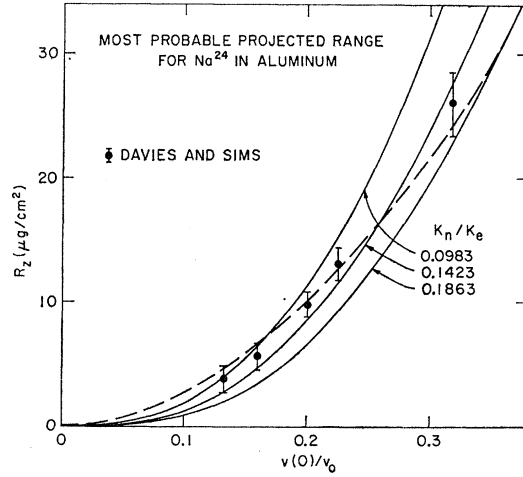[53] D. Powers and W. Whaling, Phys. Rev. 126, 61 (1962).

FIG. 20. The most probable projected range for Na[24] ions stopping in aluminum. The data points are from Ref. 55 (see also Refs. 56 and 57). The solid curves are fits of $R_z=\alpha v(0)\{1-[\arctan\gamma_i^{(1)}]/\gamma_i^{(1)}\}$, i.e., Eq. (B12a) with $m=1$, to the experimental points. The dashed curve is a fit of $R_z=\alpha v(0)\{1-[\ln(1+\gamma_i^{(0)})]/\gamma_i^{(0)}\}$, i.e., Eq. (B12a) with $m=0$. In both cases $\gamma_i^{(m)}$ is given by Eq. (B12c) and $-M_1(dv_z/dt)$ by Eq. (B11). In fitting the data the highest velocity point was strongly weighted and K_e was constrained at 2.29 keV cm²/μg.

for R_z, while if m is not an integer the integral must be solved numerically. The solution for $m=1$ has been given previously.[27] (We define $K_n^{(1)}=K_n$, $\gamma_i^{(1)}=\gamma_i$ to agree with previous notation.) Powers and Whaling[53] have measured mean projected ranges of Ne ions stopping in Be and C and N ions stopping in Be, C, and Al for ion velocities in the range $0.3\leqslant v(0)/v_0\leqslant1.0$. (In this velocity range the distinction between most probable and mean projected ranges is small and can be neglected.) We have fitted these data with the expression for R_z of Eq. (B12) with $m=1$ to obtain information on the nuclear stopping and scattering. The electronic stopping parameters K_e and α were evaluated using the procedures of Sec. 2 of this Appendix, i.e., they were obtained from the measurements of Refs. 45–48. From this fitting procedure we have found that in all five cases the value of K_n obtained by setting it equal to Bohr's estimate of the nuclear scattering at $v=v_0$ results in R_z versus $v(0)/v_0$ curves in good agreement with experiment.[54]

In Fig. 20 we show fits of R_z to range measurements of Davis and Sims[55–57] for Na[24] ions stopping in Al. The three solid curves are for $m=1$, i.e., $-M_1(dv_z/dt)_n=K_n(v_z/v_0)^{-1}$. These curves correspond to the same value of K_e, 2.29 keV cm²/μg (see Sec. 2 of this Appendix); thus they differ in K_n only. The middle

[54] A fit of Eq. (B12) with $m=1$ to the range data of Powers and Whaling for N ions in Be is shown in Fig. 8 of Ref. 27.

[55] J. A. Davies and G. A. Sims, Can. J. Chem. 39, 601 (1961); J. A. Davies, J. D. McIntyre, and G. A. Sims, ibid. 39, 611 (1961).

[56] The uncertainties in the range measurements of Davies and Sims have been arbitrarily increased to include systematic errors of the type discussed in Ref. 57.

[57] F. Brown and J. A. Davies, Can. J. Phys. 41, 844 (1963).

curve corresponds to the same value of K_n, 0.32 keV cm^2/μg, as the $K_n(v_z/v_0)^{-1}$ curve of Fig. 19. Thus we see that these range measurements for $0.1 \lesssim v(0)/v_0 \lesssim 0.3$ are reproduced fairly well by assuming the same K_n value as is extracted for $v(0)/v_0 \gtrsim 1$ from the Bohr or Lindhard-Scharff-Schiøtt estimate of $(dE/dx)_n$.

The dashed curve of Fig. 20 corresponds to $m=0$ in Eqs. (B11) and (B12). The R_z curves for $m=0$ and 1 are seen to give somewhat comparable fits to the projected range measurements. From inspection of Fig. 20 it would appear than $m \simeq 0.5$ would give a better fit than either. This indicates that for $v(0)/v_0 \lesssim 0.3$, $K_n^{(0.5)}(v_z/v_0)^{-0.5}$ could be a better representation of $-M_1(dv_z/dt)_n$ than $K_n(v_z/v_0)^{-1}$.

It should be emphasized that each range measurement corresponds to a different value of $v(0)/v_0$ and thus to a different $-M_1(dv_z/dt)$ versus v_z/v_0 curve. Each of these curves can be estimated by applying the scattering correction, via dv_z/dv, to the estimate of (dE/dx). For the reasons stated previously, this correction is such that Eq. (B11) with $m=1$ and K_n constant gives a fairly good representation of a R_z versus $v(0)/v_0$ curve. It should be noted however that because R_z is obtained from an integral, the functional form of the nuclear stopping and scattering is not determined well from range measurements. We can only say that the range data we have considered are consistent with our representation of $M_1(dv_z/dt)$ and yield an effective parameter K_n which is consistent to $\sim 25\%$ with that obtained by setting it equal to Bohr's estimate of $-(dE/dx)_n$ at $v=v_0$.

It is our contention that the parameter $K_n^{(m)}$ chosen to reproduce R_z is also close to the proper effective parameter to use in $F(\tau)$ and $dN(V)/dV$; so that the uncertainty in DSAM analysis due to uncertainties in the functional form of the nuclear effects are minimized, in our approach, by fixing $K_n^{(m)}$ from range measurements. A more direct and therefore preferable way of determining the effective parameter K_n is from measurements of $dN(V)/dV$. This method we shall now consider.

5. Application to the Doppler-Shift Attenuation Method

In this section we present the expressions for $dN(V)/dV$ and $F(\tau)$ which result from the phenomenological form for $M_1(dv_z/dt)$:

$$-M_1(dv_z/dt) = K_n(v_z/v_0)^{-1}$$
$$+K_e(v_z/v_0) - K_3(v_z/v_0)^3. \quad \text{(B13)}$$

The term $K_3(v_z/v_0)^3$ is added to take account of the variation of $(dE/dx)_e$ from $K_e(v_z/v_0)$ for $v_z \gtrsim Z_1^{2/3}v_0$. Addition of this term has been found to result in a good approximation to $(dE/dx)_e$ in the range $v_z/v_0 \lesssim 6$ for most Z_1, Z_2 combinations.[21,28] The frequency distribu-

tion corresponding to Eq. (B13) is[58]

$$\frac{dN(V)}{dV} \propto \frac{xV[\gamma_i^{-2}+V^2]^{\frac{1}{2}x-1}}{\{1-[C_i\gamma_i^2/(1+\gamma_i^2+C_i\gamma_i^2)]V^2\}^{\frac{1}{2}x+1}}$$
$$+\left[\frac{1+\gamma_i^2+C_i\gamma_i^2}{(1+C_i)(1+\gamma_i^2)}\right]\gamma_i^{-x}\delta(V), \quad \text{(B14)}$$

where $V=v_z(t)/v(0)$, $x=\alpha/\tau$, $\alpha=M_1v_0/K\rho$, and $\gamma_i^2 = [(K+K_e)/2K_n][v(0)/v_0]^2$. C_i is given by

$$C_i = \frac{K-K_e+2K_3[v(0)/v_0]^2}{K+K_e-2K_3[v(0)/v_0]^2}$$

and K is defined by $K=(K_e^2+4K_nK_3)^{1/2}$. The attenuation factor $F(\tau)$ corresponding to Eq. (B13) is[59]

$$F(\tau) = \frac{x\gamma_i^x(1+C_i)(1+\gamma_i^2)}{(1+\gamma_i^2+C_i\gamma_i^2)^{\frac{1}{2}x+1}}I(x,C_i,\gamma_i^2), \quad \text{(B15)}$$

where the integral $I(x,C_i,\gamma_i^2)$ is

$$I(x,C_i,\gamma_i^2)$$
$$=\int_0^1 \frac{V^2[\gamma_i^{-2}+V^2]^{\frac{1}{2}x-1}dV}{\{1-[C_i\gamma_i^2/(1+\gamma_i^2+C_i\gamma_i^2)]V^2\}^{\frac{1}{2}x+1}}. \quad \text{(B16)}$$

For $K_3=0$, which is a valid approximation in the present studies, $C_i=0$, $K=K_e$, and $\gamma_i^2=(K_e/K_n)[v(0)/v_0]^2$. In this case $dN(V)/dV$ and $F(\tau)$ reduce to expressions given previously.[21,27,28]

For $K_3=0$, both $F(\tau)$ and $dN(V)/dV$ are functions of two variables, α/τ and γ_i^2. In the analysis of the Doppler shift measurements presented in this paper, $F(\tau)$ was calculated (computer) from Eq. (B15) with $C_i=0$ for different values of α/τ and γ_i^2 and then values of τ corresponding to given values of α and γ_i^2 were obtained by comparing the calculated and measured values of $F(\tau)$.

Before comparing Eq. (B14) to experiment the response function of the γ-ray detector was folded into it. That is, the function compared to experiment was

$$[dN(V)/dV]_{th}$$
$$=C_N \int_0^1 [dN(W)/dW]f(W-V)dW. \quad \text{(B17)}$$

For the detector response, we used

$$f(W-V) = \exp\{-[(W-V)/\sigma]^2\}.$$

The constants C_N and σ were fixed by comparison to

[58] Equation (B14) replaces Eq. (8) of Ref. 21 which is in error unless $C_i=0$. Equation (10) of Ref. 21 is correct.
[59] Equation (B15) replaces Eq. (4) of Ref. 28 which (inadvertently) is for $K_n=0$, i.e., no nuclear stopping and scattering. Equation (B15) reduces to Eq. (4) of Ref. 28 in the limit as $K_n \to 0$.

experiment as explained in Sec. V. Equation (B17) was solved numerically (computer) for a net of values of γ_i^2 and x. For each γ_i^2, x combination X^2, representing the goodness of fit, was evaluated from

$$X^2 = N_D^{-1} \sum_j \frac{\{[dN(V)/dV]_{\text{th}(j)} - [dN(V)/dV]_{\text{exp}(j)}\}^2}{\Delta_j},$$

(B18)

where the sum is over the N_D+2 channels included in the fit (see Sec. V and Figs. 12 and 13). N_D represents the degrees of freedom. $[dN(V)/dV]_{\text{th}(j)}$ is evaluated at the velocity V corresponding to the jth channel where the experimental frequency distribution $[dN(V)/dV]_{\text{exp}}$ has the value $[dN(V)/dV]_{\text{exp}(j)}$. The weight of the jth point in Eq. (B18) Δ_j was taken as the square of the statistical uncertainty in $[dN(V)/dV]_{\text{exp}(j)}$ evaluated from the magnitude of $[dN(V)/dV]_{\text{exp}(j)}$ and the magnitude of its background. Once the net of X^2, γ_i^2, x values was determined, the best solutions for γ_i^2 and x were easily extracted (see Sec. V and Fig. 14).

An estimate of the uncertainty attached to our treatment of nuclear stopping and scattering was made in the following manner. The analytical form for $dN(V)/dV$ resulting from Eq. (B11) with $m=0$ was substituted into Eq. (B17) and the line shape of the $1.528 \rightarrow 0$ transition was fitted in the same manner as for $m=1$. In this case $K_n^{(0)}$ was constrained to $1.45NS_n^0$ keV cm²/μg, the value which gave the fit to R_z shown in Fig. 20. For Na^{22} ions stopping in CaF_2 this is 1.77 keV cm²/μg. The best fit to the experimental line shape was about one standard deviation worse than that of Fig. 12 and gave a mean lifetime for the 1.528-MeV level of 2.66 psec, 30% lower than the value obtained for $m=1$ (Fig. 12). The assumption $-M_1(dv_z/dt)_n = K_n^{(0)}$, independent of v_z, is in gross violation of the Lindhard-Scharff-Schiøtt estimate of $(dE/dx)_n$. For instance, in the case of Na^{24} ions in Al with $v(0)/v_0 = 1.3$ (Fig. 18) it gives $-(dE/dx)_n = 1.86$ keV cm²/μg which at $v(0)/v_0 = 1.3$ is 7.8 times the Lindhard-Scharff-Schiøtt estimate and $\sim 60\%$ of $(dE/dx)_e$. In view of this, the fact that the lifetime of the 1.528-MeV level is only 30% lower for $m=0$ than for $m=1$ in Eq. (B11) indicates that lifetimes extracted via the DSAM are indeed quite insensitive to the dependence of (dv_z/dt) on v_z/v_0 as long as an effective parameter is evaluated from R_z or $dN(V)/dV$.

In this Appendix we have presented a phenomenological representation of the energy loss and scattering of ions in matter which is represented by two parameters for $v(0)/v_0 \lesssim 2$ and three parameters for $2 \lesssim v(0)/v_0 \lesssim 6$. Alternate approaches to analysis of DSAM results have recently been presented.[52,60] Both of these explicitly separate the effects of scattering and of energy loss, use $K_e(v/v_0)$ to represent $(dE/dx)_e$, and use the estimates of $(dE/dx)_n$ we have considered.

We have compared our analysis to that of Blaugrund[52] by reanalyzing DSAM results obtained[61] for the Ca^{41} 1.95-MeV level. The experiment used the $K^{41}(p,n)Ca^{41}$ reaction and measurements of $F(\tau)$ were obtained with $v(0)/v_0 = 0.27$ and Ca^{41} ions stopping in C and KCl. Singh et al.[61] assumed K_e was given by Eq. (B5) in both cases and evaluated $F(\tau)$ versus τ using procedures developed by Blaugrund.[52] These authors obtained mean lifetimes for the Ca^{41} 1.95-MeV level of $(4.4_{-1}{}^{+3}) \times 10^{-13}$ sec and $(5.0_{-1}{}^{+3}) \times 10^{-13}$ sec from the values for $F(\tau)$ obtained for the Ca^{41} ions stopping in C and KCl, respectively. Using their measurements of $F(\tau)$, K_e from Eq. (B5), and K_n equal to Bohr's estimate of $(dE/dx)_n$ at $v(0)/v_0 = 1$, our analysis gives mean lifetimes of $(4.4_{-1.3}{}^{+2.1}) \times 10^{-13}$ sec and $(4.3_{-1.3}{}^{+2.1}) \times 10^{-13}$ sec, respectively. The uncertainties correspond (arbitrarily) to 15% in K_e and 25% in K_n. Thus, even for as low an initial velocity as $v(0)/v_0 = 0.27$, our analysis is in good agreement with that of Blaugrund.

APPENDIX C. γ-RAY TRANSITIONS IN F^{19} AND Ne^{22}

In this Appendix we present some results obtained for γ-ray transitions in F^{19} and Ne^{22} from the $F^{19}(\alpha,\alpha'\gamma)F^{19}$ and $F^{19}(\alpha,p\gamma)Ne^{22}$ reactions.

1. F^{19} Results

Gamma-ray transitions were observed from all three of the levels at 1.35, 1.46, and 1.55 MeV in F^{19}. The $1.35 \rightarrow 0.11$ transition, identified in Fig. 3, was found to have an energy of 1235.8 ± 0.2 keV which gives an excitation energy of 1345.7 ± 0.2 keV for the third excited state of F^{19}. The 1236-keV γ ray showed no observable Doppler effects, i.e., $F(\tau) < 0.03$, and using the procedures of Appendix B we set a limit on the mean lifetime of this level: $\tau > 8$ psec.

Three other F^{19} γ rays observed were those corresponding to the $1.55 \rightarrow 0.198$, $1.46 \rightarrow 0.110$, and $1.46 \rightarrow 0$ transitions. The first two were unresolved (Fig. 3) and the last were quite weak; thus no accurate energy measurements were made; however, some significant lifetime information was extracted by considering all three transitions. The γ rays from the decay of both the 1.46- and 1.55-MeV levels showed Doppler effects. Analysis of these effects results in a firm limit, $\tau < 5$ psec, for the mean lifetime of both the 1.46- and 1.55-MeV levels of F^{19}.

2. Ne^{22} Results

Information was obtained on the excitation energies and lifetimes of the second, third, and fourth excited states of Ne^{22} at 3.36, 4.46, and 5.14 MeV. Some of the relevant data are shown in Figs. 21 and 22. The two-escape peak of the $5.14 \rightarrow 1.27$ transition was observed

[60] R. E. Pixley and W. Benenson, Nucl. Phys. A91, 177 (1967).

[61] P. P. Singh, R. E. Segel, R. H. Siemssen, S. Baker, and A. E. Blaugrund, Phys. Rev. 158, 1063 (1967).
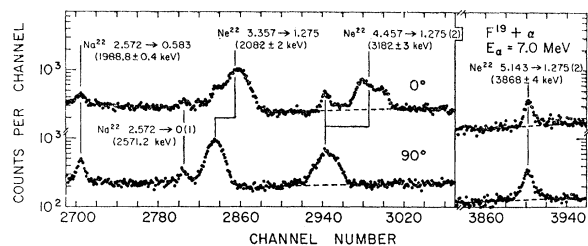
FIG. 21. Portions of two 4096-channel γ-ray spectra from bombardment of a 1.0-mg/cm² CaF₂ target with 7.0-MeV α particles. These are part of the same spectra as shown in Fig. 3. Gamma-ray peaks corresponding to transitions in Ne²² and Na²² are identified by the energies (in MeV) of the initial and final states between which the transitions take place and by the γ-ray energies in keV. One- and two-escape peaks are labeled by (1) and (2), respectively.

with $E_\alpha = 7.0$ MeV. This peak is shown in the insert to the right in Fig. 21. The full 0°–90° Doppler shift of this γ ray is calculated to be ~41 keV. No Doppler shift was observed, $F(\tau) < 0.03$, so that an upper limit was placed on the mean lifetime of the Ne²² 5.14-MeV level: $\tau > 12$ psec. The energy measurement of the 5.14 → 1.27 transition (Fig. 21) results in an excitation energy of 5.143±0.004 MeV for the fourth excited state of Ne²².

The two-escape peak of the 4.46 → 1.27 transition and the full-energy-loss peak of the 3.36 → 1.27 transition were both studied at $E_\alpha = 7.0$ MeV (Fig. 21) and $E_\alpha = 5.5$ MeV (Fig. 22). Both show Doppler effects. For the 3.36-MeV level we obtain $F(\tau) = 0.61 \pm 0.086$ and 0.52±0.073 at $E_\alpha = 7.0$ and 5.5 MeV, respectively. These values of $F(\tau)$ yield mean lifetimes of 0.35±0.11 and 0.45±0.13 psec, respectively, using the procedures of Appendix B. We adopt 0.40±0.11 psec for the mean lifetime of the 3.36-MeV level. This determination is in excellent agreement with that of Eswaran and Broude[10] who obtained 0.39±0.08 psec. The asymmetric shape of the 3.36 → 1.27 peak observed at 0° to the beam (Fig. 21) is believed to be caused by a combination of angular distribution and Doppler attenuation effects. From the energy measurement of the 3.36 → 1.27 transition we obtain an excitation energy of 3.357 ±0.002 MeV for the third excited state of Ne²².
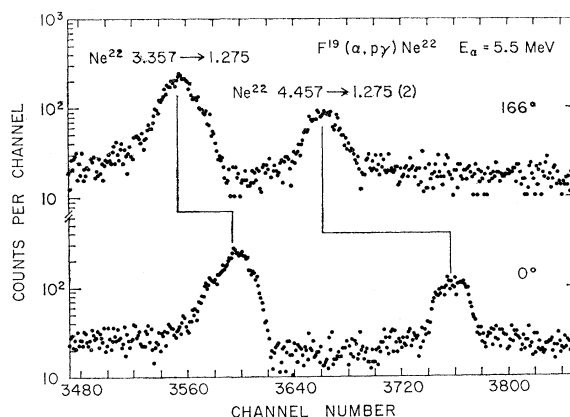

FIG. 22. The full-energy-loss peak of the Ne²² 3.357 → 1.275 transition and the two-escape peak of the Ne²² 4.457 → 1.275 transition observed at 0° (lower) and 166° (upper) to the beam following bombardment of a 1.0-mg/cm² CaF₂ target with 5.5-MeV α particles. The Ge(Li) spectra were recorded with conditions similar to that for the 0° spectrum shown in Fig. 2.

From the data obtained at $E_\alpha = 5.5$ MeV (Fig. 22) we obtain a Doppler shift for the 4.46 → 1.27 transition which is consistent with the shift calculated from the kinematics. To two standard deviations we have $F(\tau) > 0.75$, $\tau < 0.2$ psec. The same upper limit on the mean lifetime is obtained from the data recorded at $E_\alpha = 7.0$ MeV when due account is taken of the 5.14 → 4.46 cascade reported[9] to be a $(45 \pm 5)\%$ branch. Feeding of the 4.46-MeV level by this cascade is assumed to give rise to the unshifted portion of the 4.46 → 1.27 peak observed at 0° to the beam (Fig. 21). The asymmetric shape of the remaining portion of this peak is believed to be caused by the angular distribution of the reaction. Our limit, $\tau < 0.2$ psec, for the 4.46-MeV level is consistent with, but considerably weaker than, the limit $\tau < 0.035$ psec quoted by Eswaran and Broude.[10] The energy measurement of the γ ray corresponding to the 4.46 → 1.27 transition (Fig. 21) results in an excitation energy of 4.457±0.003 MeV for the third excited state of Ne²².

In summary we find the following values of (E_x, τ) for the second, third, and fourth excited states of Ne²²: (3.357±0.002 MeV; 0.40±0.11 psec), (4.457±0.003 MeV; <0.2 psec), and (5.143±0.004 MeV; >12 psec).